



TECHNICAL ARTICLE

Insights on Microstructure and Failure Characteristics of Resistance Spot Welds of Galvannealed Dual Phase Steel

Kaushal Kishore , Pankaj Kumar, and Goutam Mukhopadhyay

Submitted: 19 September 2021 / Revised: 7 April 2022 / Accepted: 25 April 2022 / Published online: 20 June 2022

This work examines the effect of spot-welding current on the load-bearing capacity and the fracture mechanism of galvannealed dual-phase steel (DP600) joints. A greater than three-fold increase in the load-bearing capacity of the joint was achieved by increasing the welding current from 6 to 9 kA. Quantitative fractography showed a transition from predominantly transgranular cleavage fracture at 6 kA current with only ~7 dimples to ~17% ductile dimples at 7 kA current and eventually 100% ductile dimples for 9 kA current. Detailed microstructure-hardness relationship across the different welding zones is presented using scanning electron microscopy and electron backscattered diffraction techniques. At the optimized welding parameter, load-controlled fatigue tests revealed a decrease in the number of cycles to failure with increasing load amplitude, and endurance was achieved for 10% of the maximum tensile-shear load-bearing capacity. Investigation of failed specimens revealed that while under tensile loading conditions, crack initiated from the base metal, fatigue crack initiated from the heat-affected zone. Also, the possibility of different categories of liquid metal embrittlement cracks are discussed.

Keywords fatigue crack, heat-affected zone, liquid metal embrittlement, nugget diameter, resistance Spot welding

1. Introduction

In order to combat the issue of greenhouse gas emissions, automotive industries are striving for light weighing of the passenger vehicles by using thinner sheets of high-strength steel (Ref 1-3). Advanced high strength steels (AHSS) have been extensively used in automotive industries as a solution for total weight reduction, safety performance improvement, and cost-saving. Dual-phase (DP) steel is one of the most widely used AHSS in the automobile sector owing to a combination of high strength and ductility coupled with formability, toughness, and fatigue strength. A composite microstructure of ductile α -ferrite and hard martensite provides a high strength-to-weight ratio and reasonably good formability to dual-phase (DP) steel (Ref 4-6). The initial high work hardening rate with good uniform and total elongation combines to give DP steels a much higher ultimate tensile strength (UTS) and a lower ratio of yield strength (YS) to UTS than conventional steels at a

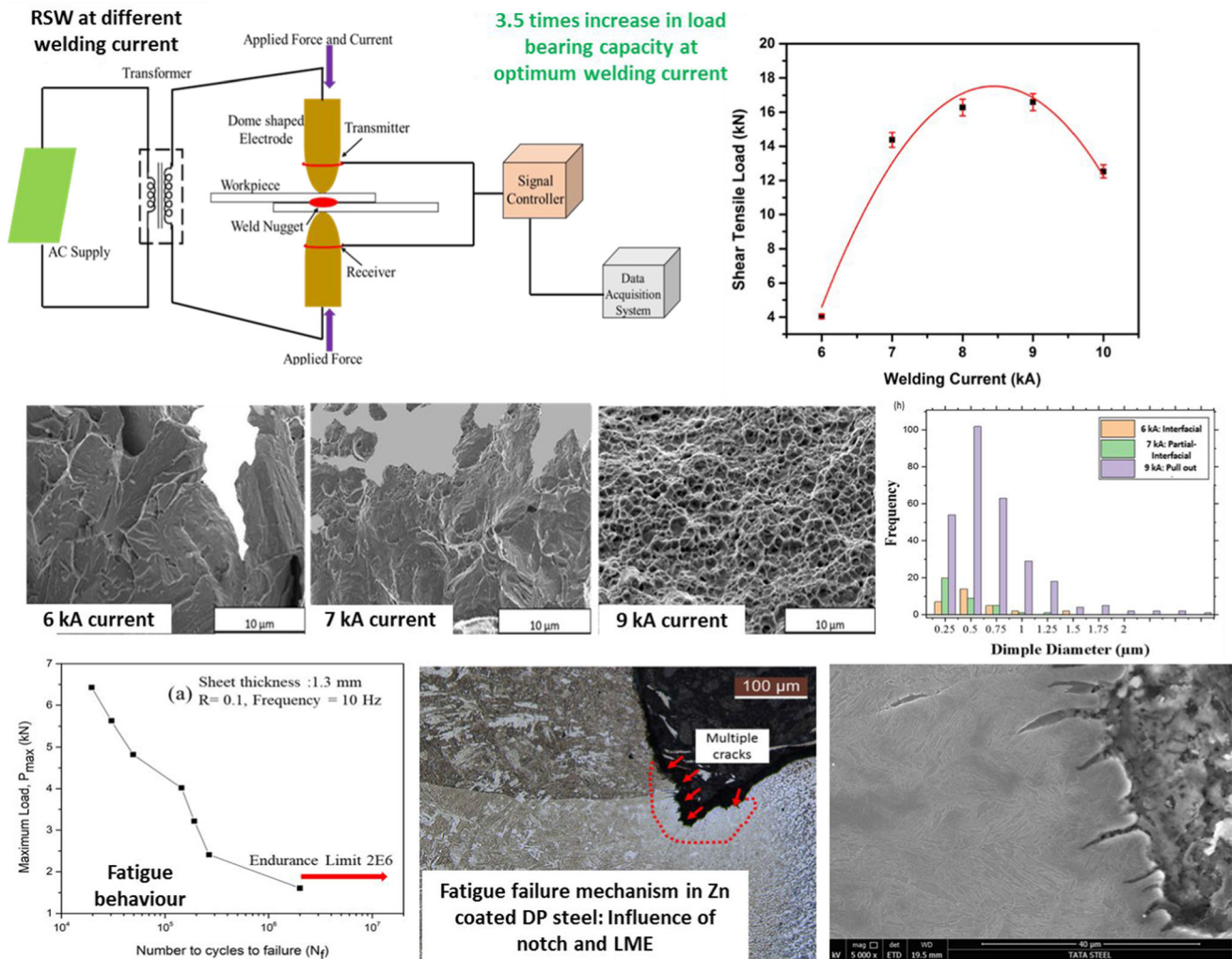
similar level of yield strength (Ref 7, 8). Despite these advantages, DP steel usually suffers from poor corrosion resistance due to low alloying content and two-phase microstructure having the potential to create galvanic coupling at the microscopic level. This is usually combated by galvanizing followed by annealing to allow inter-diffusion of zinc and iron to form alloy layer and compounds which has a superior combination of corrosion resistance and formability (Ref 9).

Industrially, to form larger components, joining sheet metals is an essential step and in the context of the automotive industry, resistance spot welding (RSW) is among the most widely used methods for joining metallic parts (Ref 10-14). While RSW possesses the advantages of being a highly efficient method with no requirement of filler electrode, relatively narrow heat-affected zone (HAZ), and a clean methodology of joining, it suffers from the disadvantages of having an inherent notch at the sheet metal interface and the point of electrode indentation, rapid degradation of the electrode and narrow processing window for optimized strength and desired mechanism of failure (Ref 15, 16). Furthermore, the RSW of coated steel sheets possess different challenges due to their higher resistivity and low melting point constituents leading to a tendency for expulsion, defect formation, and liquid metal embrittlement (Ref 17-19). To this end, Chen et al. showed that RSW of Al-Si-coated press-hardened steel led to the formation of a sharp notch in the region between sheet metal interface and the weld nugget which acted as a pre-existing crack and reduced the load-bearing capacity of the joints compared to uncoated sheets (Ref 20). Ashiri et al. demonstrated the problem of liquid metal embrittlement in Zn-coated TWIP steels (Ref 21). They highlighted that there is a supercritical area and a critical nugget diameter where the LME occurs in Zn-coated TWIP steels during RSW (Ref 21, 22).

Supplementary Information The online version contains supplementary material available at <https://doi.org/10.1007/s11665-022-07060-4>.

Kaushal Kishore and **Goutam Mukhopadhyay**, R&D and Scientific Services, Tata Steel Limited, Jamshedpur 831007, India; and **Pankaj Kumar**, National Institute of Technology, Jamshedpur 831014, India. Contact e-mail: Kaushal.kishore3@tatasteel.com.

Graphical Abstract



Further, it was revealed that the type of coating, viz., galvanized, galvanized or electro-coated Zn has an influence on the LME susceptibility. Simulation suggested that a combination of conditions, namely, temperature range where Zn exists in a molten state and mechanical stress concentration is a pre-requisite for LME to occur. However, LME in Zn-coated TWIP steel can be prevented by smart heat management through two pulse strategy involving a longer first pulse to form nugget and strong corona bond followed by a small second pulse for the nugget growth preventing LME and reducing thermal stresses (Ref 22). Likewise, RSW of galvanized 1 GPa TRIP steel revealed an increase in nugget diameter with welding current but the reduction in ductility ratio, which is explained based on the formation of defects and liquation cracks at higher heat inputs (Ref 23). Although the issue of LME is more prominent and extensively reported for coated advanced high strength steels like press-hardened steels, TWIP, and TRIP steels, Milititsky et al. elucidated the possibility of LME during RSW of DP600 steel sheets under certain conditions (Ref 24).

It is worth noting that a passenger vehicle consists of approximately 3000-5000 spot welds (Ref 25). Furthermore,

the thermal cycles during RSW involving rapid heating, solidification, and solid-state phase transformations essentially result in the destruction of the carefully engineered composite microstructure of α -ferrite and martensite obtained through prior thermo-mechanical processing (Ref 26-28). The passenger safety and the reliability of the automobile depend as much on the integrity of the welds as the parent metal itself. It has been observed that the unique state of stresses in and around spot welds joints typically causes around 70-80% of the failures whereas only about 20-30% of the failures occur in the base metal sheet away from the spot-welded joints. Despite this, a large number of literature can be found on the microstructure-mechanical property correlations for DP steel (Ref 29-32), whereas, the factors controlling the integrity of spot welds of galvanized DP steels have not received similar attention. In this regard, it has been reported that the load-bearing capacity of the RSW joints of DP 600 steel generally increases with an increase in heat input and nugget diameter until the onset of expulsion (Ref 26-28). A similar relationship between heat input, nugget diameter, and quasi-static load-bearing capacity of the RSW joints of a similar and dissimilar combination of automotive steel sheets has been reported in several recent

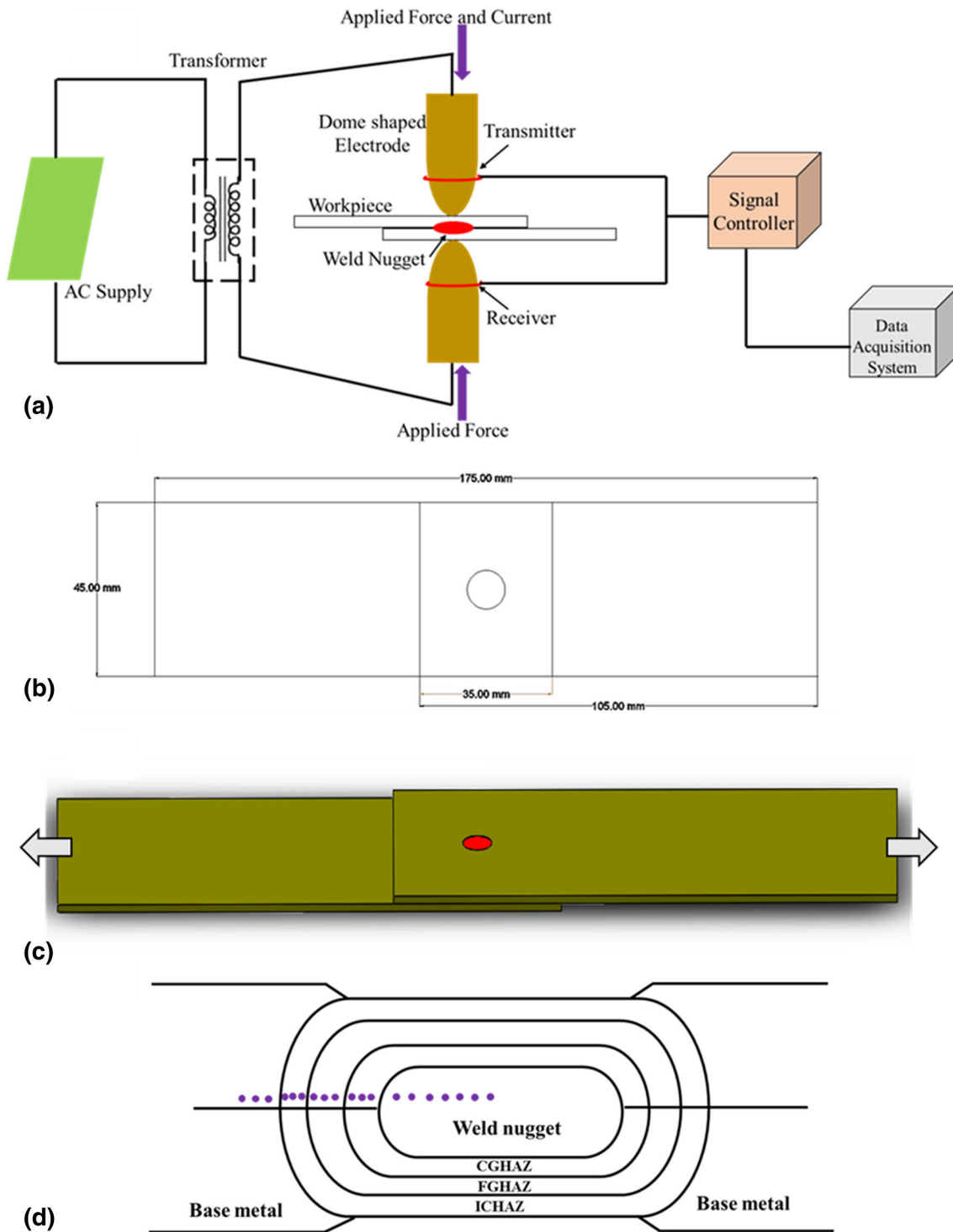


Fig. 1 (a) Schematic showing the laboratory set-up of resistance spot welding (RSW), (b) specimen configuration used for (b) welding and (c) subsequent tensile-shear and fatigue tests, (d) Schematic showing the micro-hardness measurement across different zones of resistance spot welded DP 600 steel

works (Ref 33-36). However, most of the studies have been limited to the quasi-static condition of loading and the subject of fatigue behavior of RSW joints of coated DP 600 steel has not received adequate attention. It must be noted that in practical situations, fatigue is the most likely mechanism of failure owing to large fluctuation in stresses during the service. Therefore, to bridge this gap in the literature, a systematic study

on resistance spot welding of galvanized DP 600 steel is presented here. The work consists of three essential components, namely: (i) understanding the development of microstructure and micro-hardness examination across the weld, (ii) optimizing the welding parameter with respect to tensile-shear tests, (iii) understanding the difference in failure mechanisms under tensile-shear and fatigue loading conditions

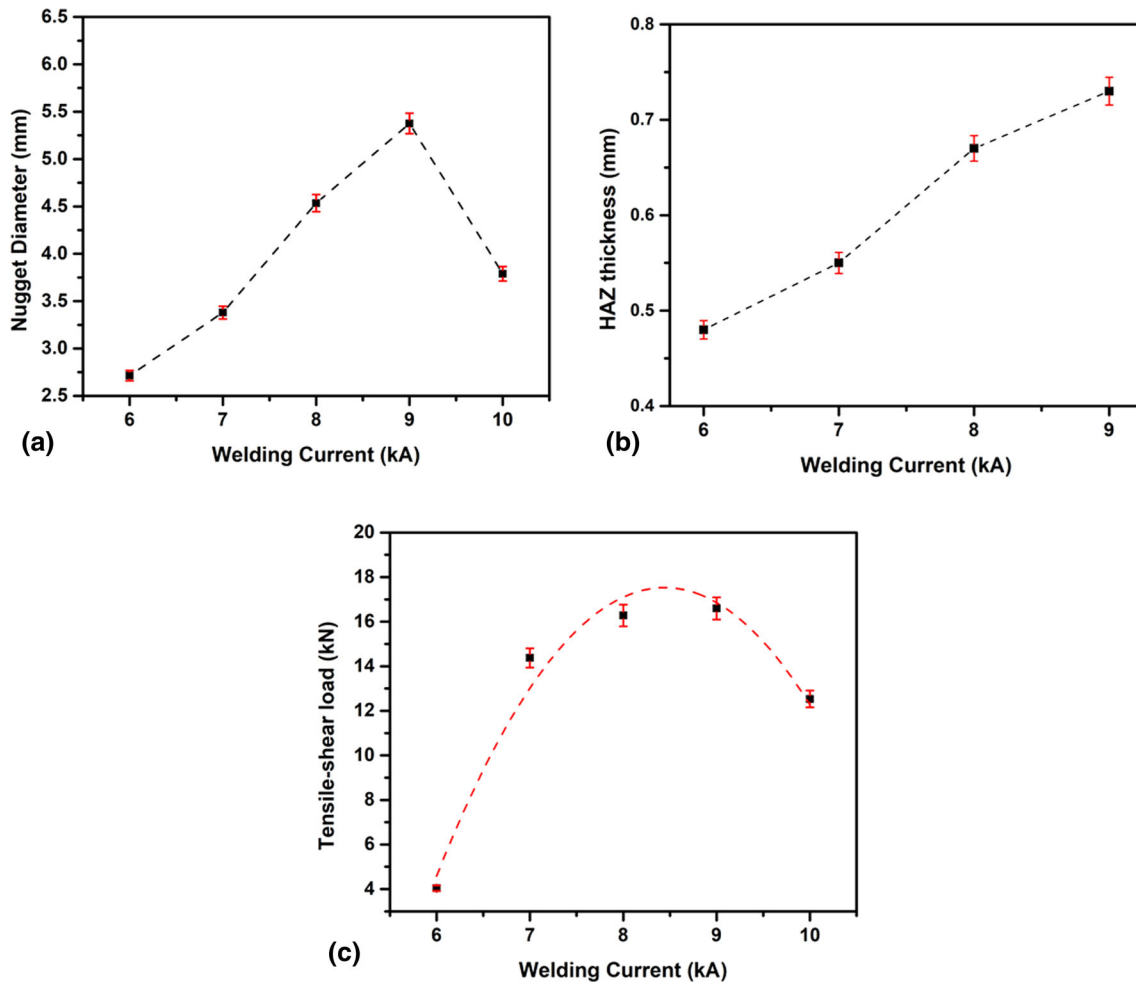


Fig. 2 Influence of welding current on: (a) nugget diameter, (b) HAZ thickness, (c) tensile-shear load-bearing capacity

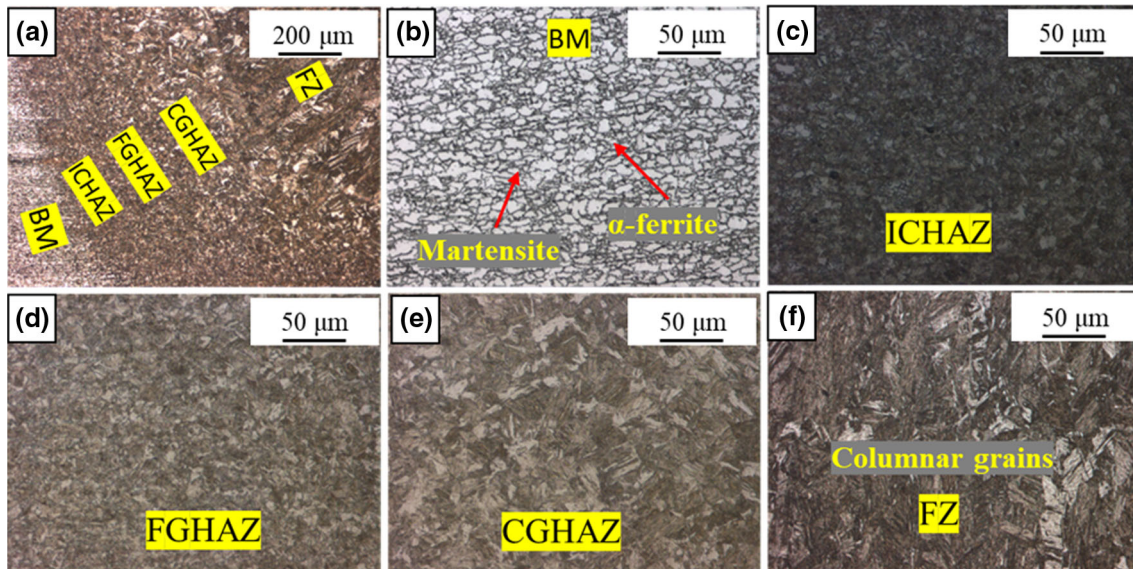


Fig. 3 Optical micrographs of different zones of resistance spot welded galvanized DP 600 steel joints: (a) macrostructure showing different zones of welding, (b) base metal, (c) intercritical heat affected zone, (d) fine-grained heat affected zone, (e) coarse-grained heat affected zone, (f) fusion zone

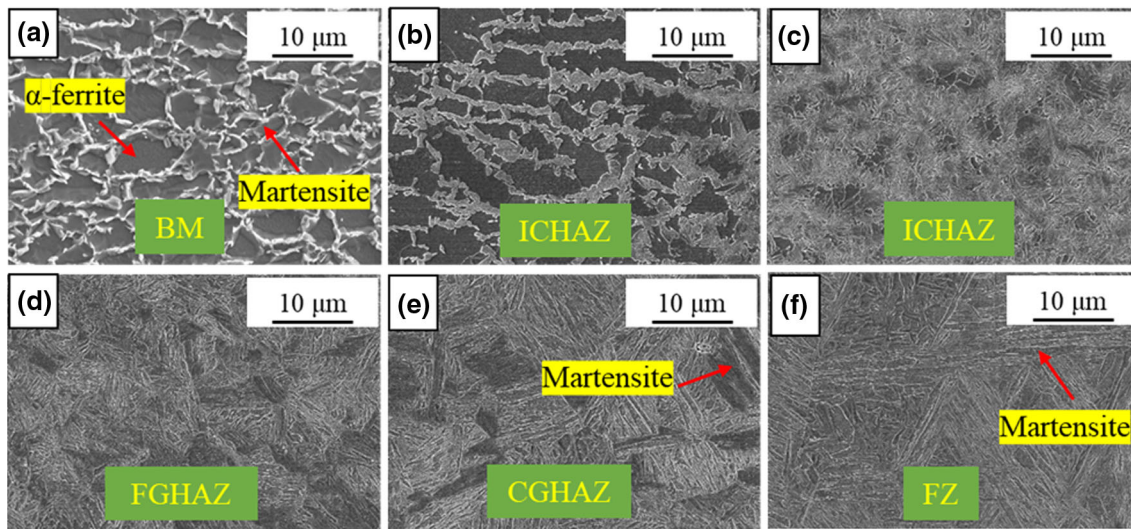


Fig. 4 Scanning electron micrographs of different zones of resistance spot welded galvanized DP 600 steel joints: (a) base metal, (b) intercritical heat affected zone closer to the base metal, (c) inter-critical heat affected zone closer to the nugget, (d) fine-grained heat affected zone, (e) coarse-grained heat affected zone, (f) fusion zone

using fractography and tracing the crack path in both the conditions. A special emphasis has been laid on identifying the possibility of liquid metal embrittlement (LME) and its role in failure mechanisms under tensile-shear and fatigue loading conditions.

2. Materials and Methods

The present study was conducted on galvanized dual-phase steel (DP 600) sheets with a thickness of 1.3 mm. DP 600 steel sheet with a nominal composition of 0.09 C-1.71 Mn-0.014 P-0.005 S-0.03 Ni-0.26 Cr-0.17 Mo-0.048 Al-0.002 V-0.02 Nb- Balance Fe was used in this study. The chemical composition of the steel sheet was determined using induction coupled plasma (ICP) and optical emission spectroscopy (OES) techniques. Steel sheet had a yield strength of 390 ± 9 MPa, the ultimate tensile strength of 635 ± 10 MPa, and total elongation of $24 \pm 2\%$.

Figure 1(a) depicts the schematic of the RSW process. It uses a 150 kVA pedestal-based welding machine having an alternating current source. The dome-shaped electrode having a tip diameter of 6 mm and made of Cu-Cr-Zr alloy which is water-cooled is used to apply the mechanical force and causes resistance heating to join the materials by forming nugget. The spot welding of DP 600 steel has been carried out in lap configuration as per BS1140:1993 standard (Ref 37) as shown in Fig. 1(b). In the present study, electrode force and welding time are kept constant at 2.8 kN and 300 ms respectively and the welding current is varied from 6 to 10 kA. The effect of welding current on the nugget diameter was established by its measurement using a stereomicroscope. Metallographic samples were prepared by cutting along the cross section of the nugget, followed by a standard polishing technique to achieve a scratch-free mirror finish specimen. These were etched using a 3% nital solution for metallography. Subsequently, microstructural examination across different zones of welding was carried out using optical (Leica, DMI 5000M) and scanning electron microscopes (Zeiss Supra 25). Scanning electron microscopy

was carried out at an accelerating voltage of 15 kV and the working distance was kept at 14.5 mm. Electron backscattered diffraction (EBSD) of different zones of welding was conducted with a tolerance angle of 1° and a step size of $0.02 \mu\text{m}$. To determine the local variation in mechanical properties across the welding zones, micro-hardness measurements were conducted using Vickers hardness testing machine (model: Durascan 20). To ascertain the influence of welding current on the load-bearing capacity, tensile-shear tests were carried out as shown schematically in Fig. 1(c). Tests were carried out on an Instron testing machine (Model: 5582) at a cross-head velocity of 5 mm/min at room temperature. At each welding parameter, a minimum of three shear-tensile tests was conducted for statistical confidence. The samples were tested using grips with flat jaw faces. Failure modes were identified using visual observation and fractography was carried out to determine the mechanism of failure. Based on maximum load in shear-tensile tests and failure modes (pullout failure mode is preferred because of higher toughness), the optimum spot-welding parameter was determined.

The hardness values were measured from the base metal to welded zone at regular intervals. Measurement of the hardness of various zone was carried out using a load of 100 gmf with an indentation duration of 15 s as shown in Fig. 1(d).

Fatigue tests were carried out to determine the number of cycles to failure at various percentages of maximum load at optimum welding parameters. Based on the maximum load, the welded samples were tested under cyclic loading conditions in a resonance-based fatigue testing machine (INSTRON 8801) with a maximum dynamic amplitude of ± 50 kN and a frequency range of (40-400 Hz). The samples were subjected to sinusoidal load with $R=0.1$ and a frequency of 5 Hz.

Fractographic examination of fatigue failed specimen was carried out under SEM with the working distance between 28 and 31 mm for greater depth of focus and an accelerating voltage of 20 kV was used. To determine the mechanism of crack initiation and growth in tensile-shear and fatigue conditions, macro and microstructure examinations of the failed specimen were carried out. Energy-dispersive spec-

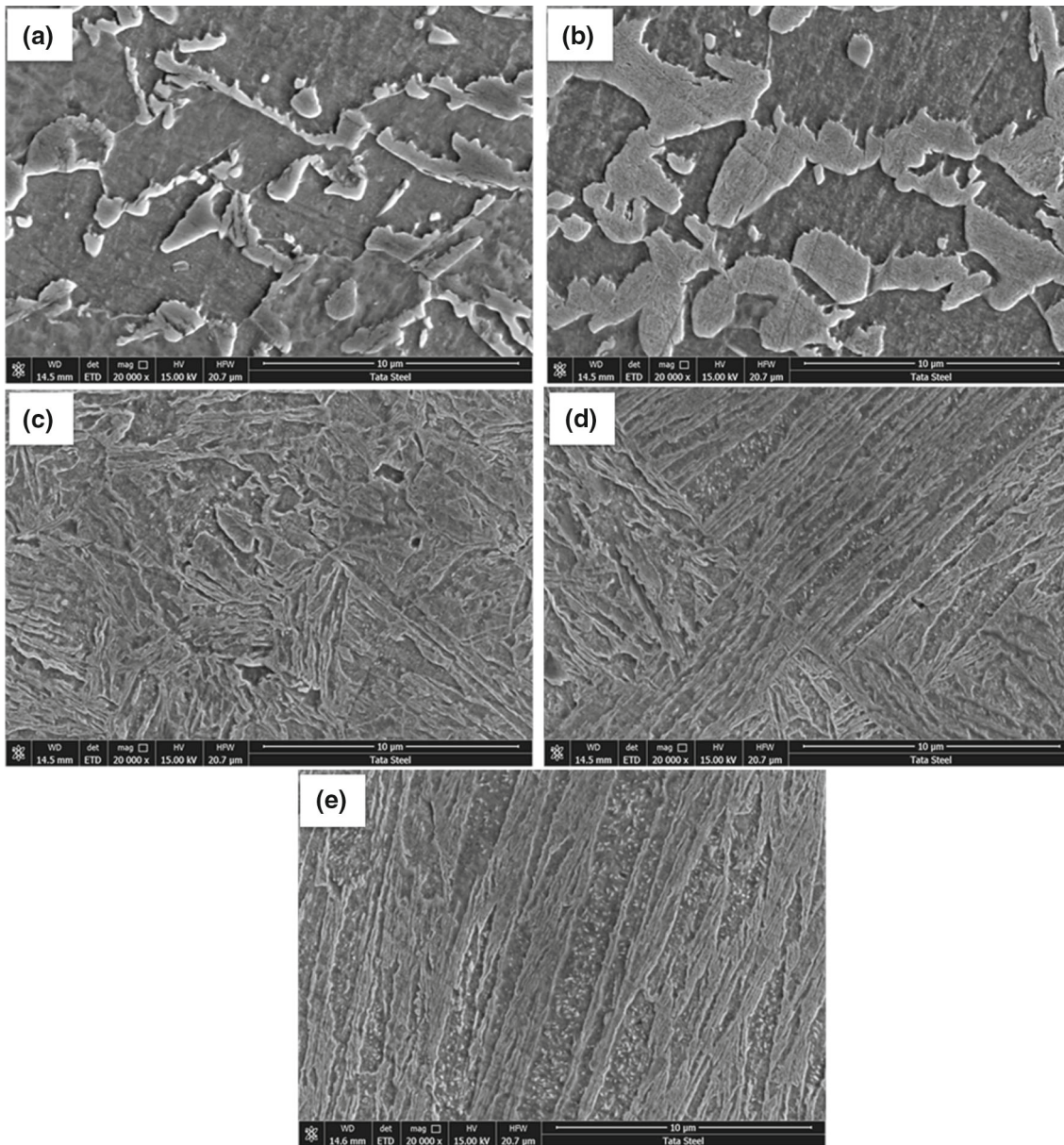


Fig. 5 Higher magnification SEM micrographs of different zones of welding: (a) base metal, (b) ICHAZ, (c) FGHAZ, (d) CGHAZ, (e) fusion zone

troscopy (EDS) mapping was carried out to aid the investigation with respect to the possibility and mechanism of LME. During EDS analysis, a higher accelerating voltage of ~ 30 kV was used and the working distance was kept between 19 and 23 mm.

3. Results and Discussion

3.1 Influence of Welding Current on Nugget Diameter and Tensile-Shear Behavior

It is evident from Fig. 2(a) that nugget diameter initially increases with an increase in welding current till 9 kA and then goes down. The increase in nugget diameter is associated with the higher heat input ($H = I^2 R t$) which results in melting and subsequent solidification of the greater mass of the sheet metals

and therefore formation of a larger fusion zone or the so-called nugget. However, at 10 kA welding current, the heat input reaches a threshold value that is so large that expulsion occurs. The event of expulsion is associated with the ejection of a significant amount of liquid metal outside the nugget which effectively reduces the nugget diameter. Similarly, HAZ thickness increases with an increase in welding current as shown in Fig. 2(b). Figure 2(c) shows the variation of tensile-shear load bearing capacity as a function of welding current. Similar to the variation of nugget diameter, load-bearing capacity increases first and then decreases corresponding to expulsion. A similar effect of nugget diameter on the tensile-shear load-bearing capability has been reported for a large number of similar and dissimilar spot welds of automotive steel grades (Ref 35, 38-40). However, for higher strength martensitic steels, load-bearing capacity does not necessarily increase with nugget diameter even before expulsion due to significant

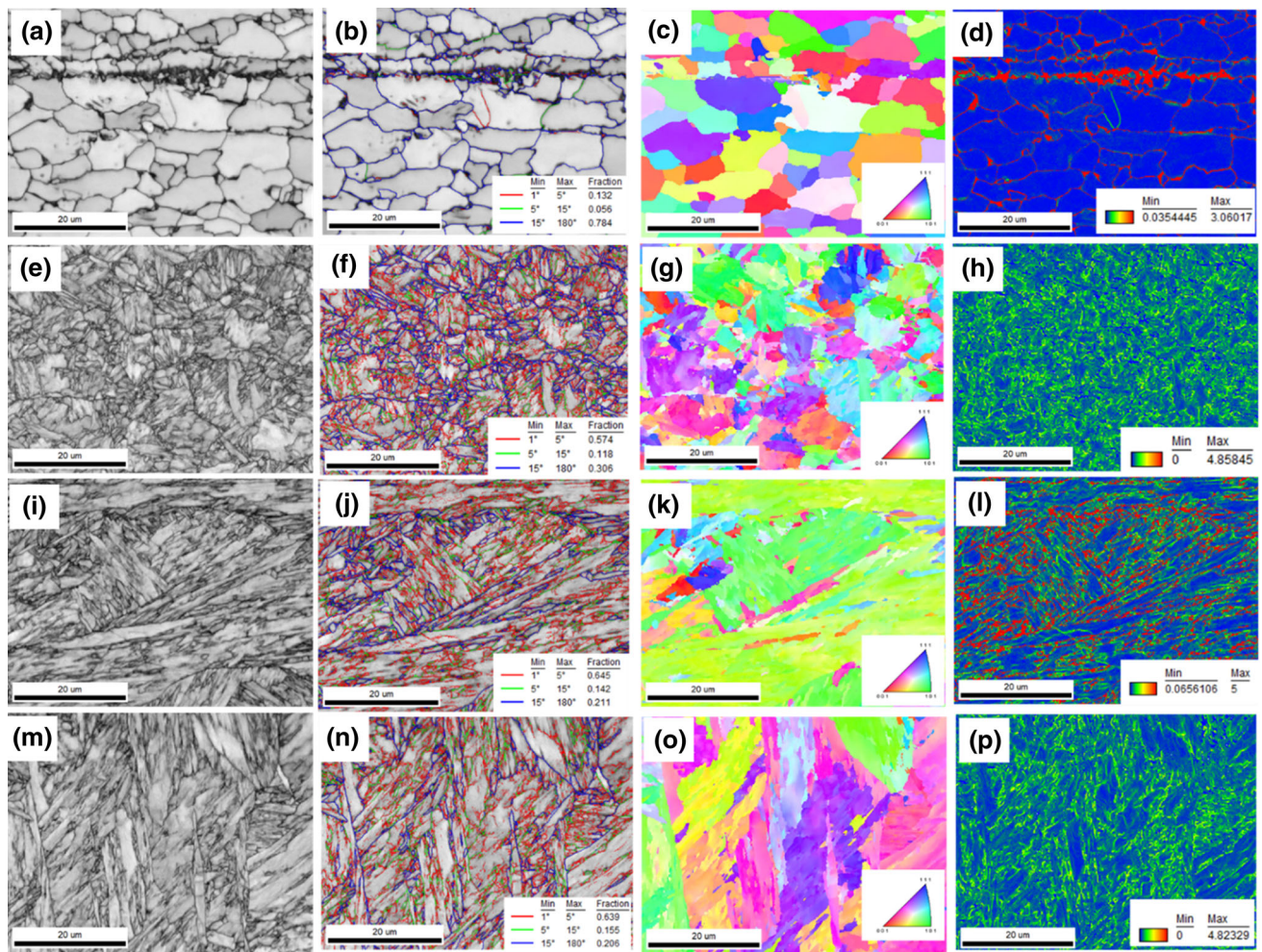


Fig. 6 Electron backscattered diffraction analysis of different zones of welding showing image quality (IQ) map, IQ map superimposed with boundary characters, inverse pole figure (IPF) map, Kernel average misorientation (KAM) map respectively for: (a-d) base metal, (e-h) FGHAZ, (i-l) CGHAZ, (m-p) fusion zone

softening of martensite in the heat-affected zone at higher current values (Ref 41). It is worth noting that an increase in welding current from 6 to 9 kA resulted in a more than a three-fold increase in the load-bearing capacity. 9 kA welding current resulted in the maximum tensile-shear load of ~ 17 kN. This parameter of welding has been used for subsequent microstructural examination and setting parameters for load-controlled fatigue tests.

3.2 Microstructural Characterization of the Weld

A cross section macrograph of different zones of resistance spot welding is presented in Fig. 3(a). Five different zones are identified, which are: (i) base metal (BM), (ii) intercritical heat affected zone (ICHAZ), (iii) fine-grained heat affected zone (FGHAZ), (iv) coarse-grained heat affected zone (CGHAZ) and (v) fusion zone (FZ). BM which does not experience any microstructural changes shows fine-grained structure. HAZ undergoes solid-state phase transformations and consequently, a different morphology was observed compared to BM. Depending on the peak temperature and cooling rate experienced at various locations, HAZ is classified as ICHAZ, FGHAZ, and CGHAZ. The location where the melting and

resolidification of sheet metals occur is the fusion zone (FZ) or the nugget. The microstructure of the BM is shown in Fig. 3(b). It consists of a α -ferrite matrix with $\sim 15\%$ martensite. This is typical of DP 600 steel. In all the heat-affected zones, the exact morphology could not be determined from the optical micrographs. However, the microstructural features are finer in FGHAZ compared to CGHAZ as shown in Fig. 3(d) and (e), respectively. Microstructure in the fusion zone presented in Fig. 3(f) revealed the presence of columnar morphology typical of directional solidification. SEM micrographs of different zones of welding are presented in Figure 4 and 5. Base metal consists of both intergranular and intragranular martensite in the α -ferrite matrix as shown in Fig. 4(a). The fraction of martensite in the ICHAZ is a function of the peak temperature. The higher the peak temperature within the intercritical range, the higher is the fraction of austenite, which transforms to martensite during the cooling. Consequently, ICHAZ closer to the fusion zone (Fig. 4c) has a much higher fraction of martensite compared to that adjacent to the base metal (Fig. 4b). Both FGHAZ and CGHAZ, essentially consisted of martensite as shown in Fig. 4(d) and (e), respectively. However, the lath size and prior austenite grain size are finer in FGHAZ compared to CGHAZ. This is again because the peak

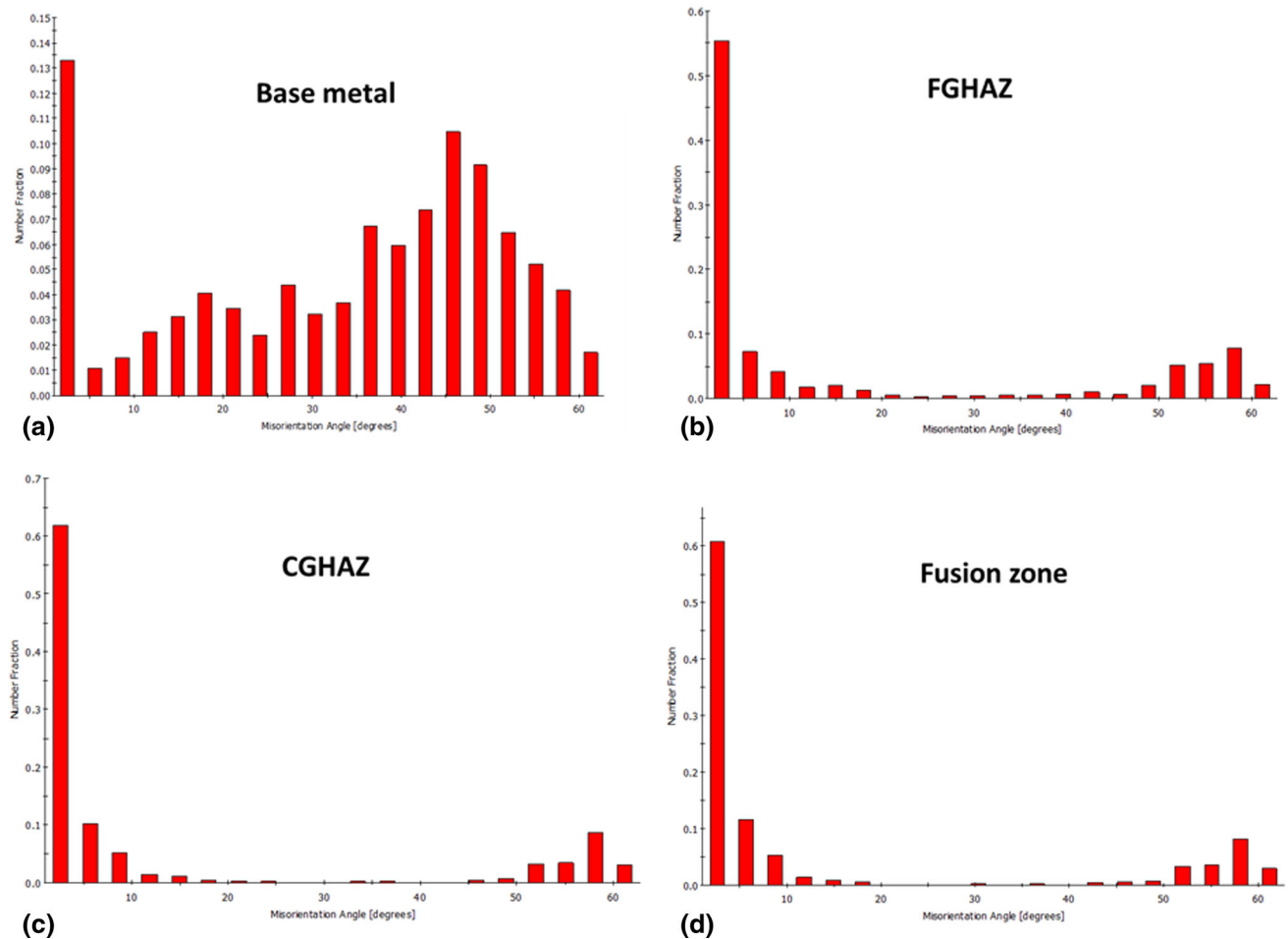


Fig. 7 Variation of misorientation angles in different zones of welding: (a) base metal, (b) FGHAZ, (c) CGHAZ, (d) Fusion zone

temperature in CGHAZ is greater than that in FGHAZ. Furthermore, FGHAZ experiences a greater cooling rate as it is closer to the base metal, which acts as a heat sink compared to CGHAZ which is closer to the fusion zone. The microstructure of the fusion zone (FZ) is typical of solidification and consists of lath martensite as shown in Fig. 4(f). Higher magnification microstructures of different zones of spot welds are provided in Fig. 5.

Figure 6 shows the EBSD analysis consisting of image quality (IQ) map, boundary characters, inverse pole figure (IPF) map, and Kernel average misorientation (KAM) map of different zones of the spot weld. In each zone, confidence index (CI) > 0.97 was achieved with respect to the BCC iron phase indicating good quality of indexing along with confirmation that BCC iron is the major phase. In the base metal of DP 600 steel, martensite was associated with localization of strain around it as evident from Fig. 6(d), which is consistent with the fact that it is a highly dislocated structure. Softer α -ferrite grains are having low KAM indicating lower geometrically necessary dislocations (GND) therein. FGHAZ showed a higher fraction of low angle grain boundaries (LAGB) as shown in Fig. 6(f). KAM map of FGHAZ presented in Fig. 6(h) revealed higher GND density compared to the base metal, however, it is more uniformly distributed. In contrast,

CGHAZ had a coarser martensitic structure with intense localization of strain as revealed by the KAM map shown in Fig. 6(l). This may explain the lower toughness and higher susceptibility of CGHAZ to failures. The Fusion zone showed lath martensite structure, with less severe strain localization compared to CGHAZ, as revealed by the KAM map shown in Fig. 6(p).

Variation of misorientation angles of the boundaries in different zones of welding is shown in Fig. 7. Base metal had a considerably higher fraction of high angle grain boundaries (HAGB) compared to CGHAZ, FGHAZ, and fusion zone. In HAZ and fusion zones, a very high fraction of low angle grain boundaries (LAGB) was observed, which may be attributed to a very high cooling rate in RSW due to water-cooled copper electrode resulting in martensitic microstructure and substructure formation. Such a high fraction of LAGB is corroborate with the higher KAM values in these zones compared to the base metal. A higher ratio of LAGB/HAGB is consistent with the findings of Hajiannia et al. for RSW of TRIP steel (Ref 42).

3.3 Hardness Measurements Across the Weld

Figure 8(a) shows the variation of micro-hardness on traversing from the base metal to the center of the fusion zone.

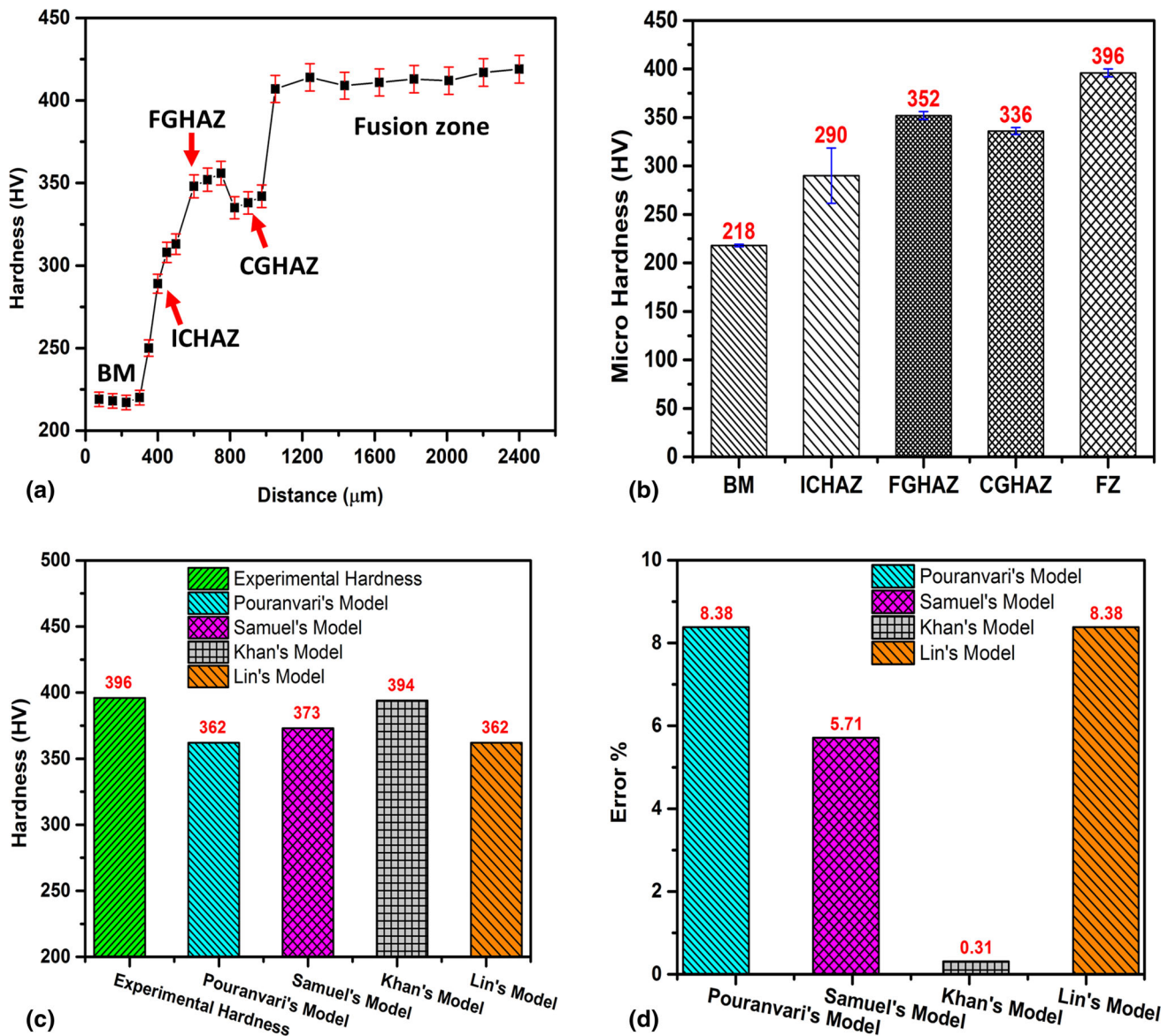


Fig. 8 (a) Hardness profile across different welding zones, (b) mean values of micro-hardness in different welding zones, (c) comparison of the experimentally determined hardness of fusion zone with those predicted by different models for the given composition of the steel (Ref 43-46), (d) accuracy of different models for prediction of the hardness of the fusion zone

Correspondence between the microstructure and the average micro-hardness values of different zones of the welding was observed. The microhardness values were observed to be maximum in the fusion zone followed by fine-grain heat affected zone, coarse grain heat-affected zone, inter-critical heat affected zone and it was the minimum in the base metal. As the volume fraction of martensite is minimum in the base metal, it showed the minimum hardness of ~ 218 HV. Within the ICHAZ, the micro-hardness values increased with an increasing fraction of martensite. The hardness of FGHAZ was higher than CGHAZ due to refined microstructure and therefore greater resistance to the movement of dislocation owing to a higher boundary fraction.

Several empirical models exist to estimate the hardness of the martensitic microstructure in the fusion zone of resistance spot welds (Ref 43-46). A comparison of experimentally

measured hardness in the FZ and those predicted by different models are summarized in Fig. 8(c). Although all the models could predict the hardness of the FZ with reasonably good accuracy with % error < 10 , it is worth noting that the value obtained from Khan's model is the closest to the experimentally determined hardness with % error as low as $\sim 0.30\%$.

3.4 Fractography after Tensile-Shear Tests

A combination of visual observations (Fig. 9) and fractography (Fig. 10) was carried out at different welding currents to understand the transition in the mechanism of failure. Fractographic examinations were carried out ahead of the crack initiation location and multiple images were captured for quantification. There was considerable variation in the mode of fracture for specimens welded at different currents as shown in

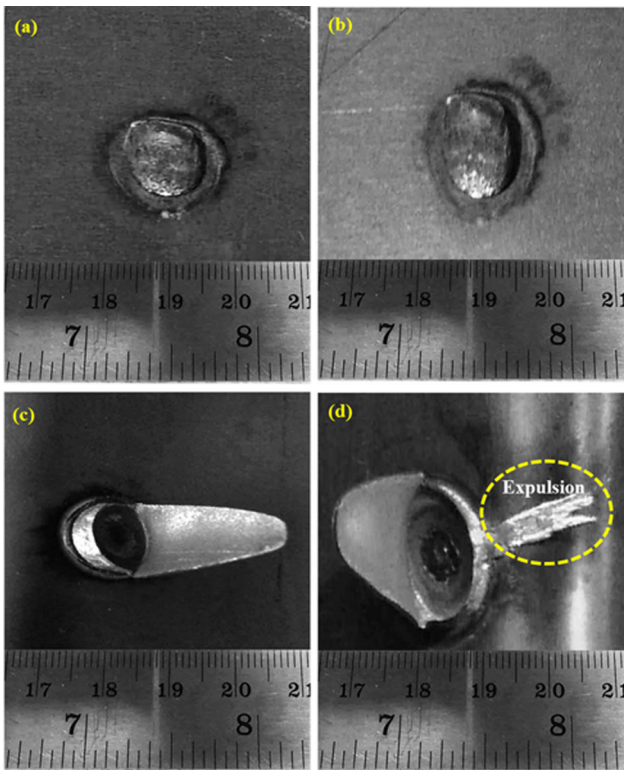


Fig. 9 Visual images of the RSW welds failed in different modes under tensile-shear tests: (a) interfacial failure (6 kA welding current), (b) partial interfacial failure (7 kA welding current), (c) pull-out failure (9 kA welding current), (d) expulsion (10 kA welding current)

Fig. 9. At 6 kA current, interfacial failure was observed where crack propagation occurred inside the nugget as shown in Fig. 9(a). This coincided with very low load-bearing capacity and fractography showed predominantly cleavage fracture as shown in Fig. 10(a). There is a very small zone of dimples in it as well which is distinguished. On increasing the welding current to 7 kA, it led to partial-interfacial failure (Fig. 9b) with a mixed mode of fracture, wherein part of the fracture surface showed cleavage planes typical of transgranular brittle fracture, whereas the other part revealed the presence of ductile dimples as shown in Fig. 10(b). The transition in fracture mode from predominantly brittle at 6 kA current to a combination of brittle and ductile fracture at 7 kA current manifested as an increase in tensile-shear load-bearing capacity from ~ 4 to 14 kN. At still higher welding current, viz., 8 and 9 kA, there was a complete pull-out failure, which is the most desirable mechanism from the viewpoint of load-bearing capacity and toughness. It resulted in completely ductile dimple formation on the fracture surface as shown in Fig. 10(c). A transition to favorable ductile pull-fracture mode is associated with the maximum load-bearing capacity of ~ 17 kN at 9 kA current. Any characterization of the welded joint that suffered expulsion at 10 kA (Fig. 9d) was abandoned as it is of no practical importance.

Image J software was used to quantify the percentage of ductile dimples in the case of the specimen that failed in interfacial, partial interfacial, and pull-out failure modes. Processed images showing ductile fracture region with different shades for 6 and 7 kA welding current samples are presented in Fig. 11(a) and (b), respectively. The area fraction of the ductile fracture zone increases from 7.6 to 17.1% on increasing welding current from 6 to 7 kA. This increase in the fraction of ductile dimples is also associated with a transition in failure

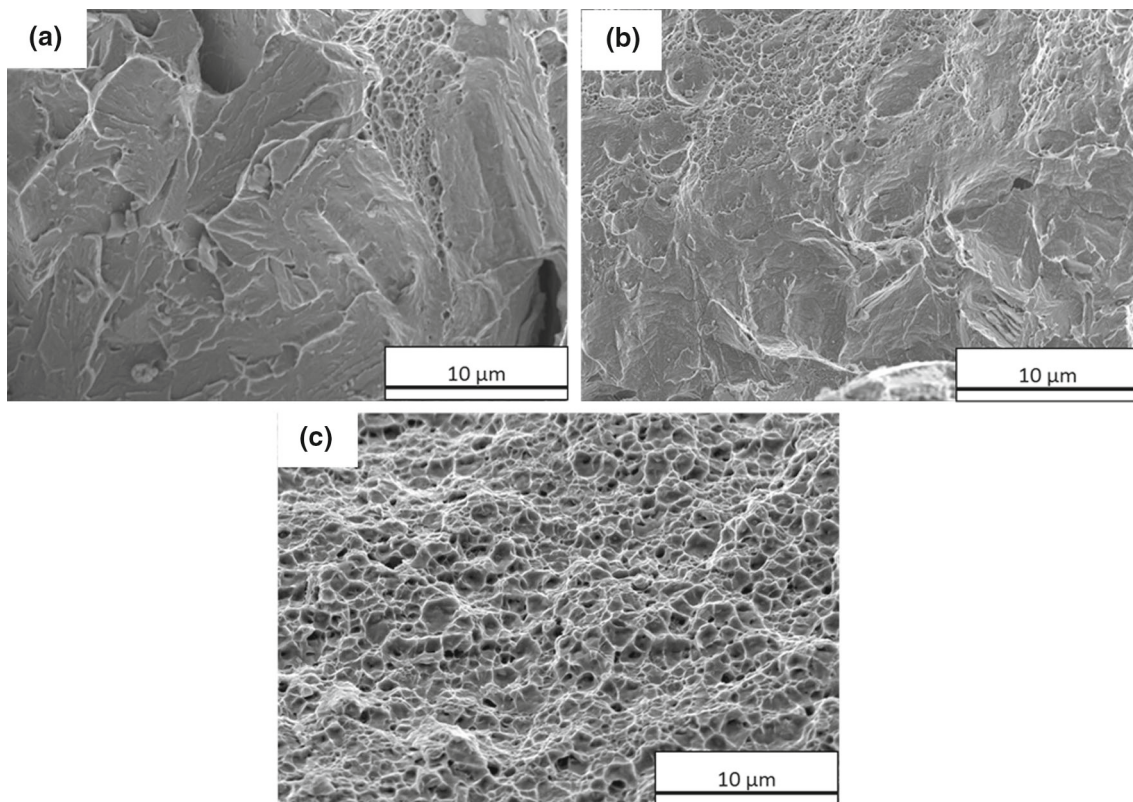


Fig. 10 SEM fractography corresponding to (a) interfacial failure, (b) partial-interfacial failure, (c) pull-out failure

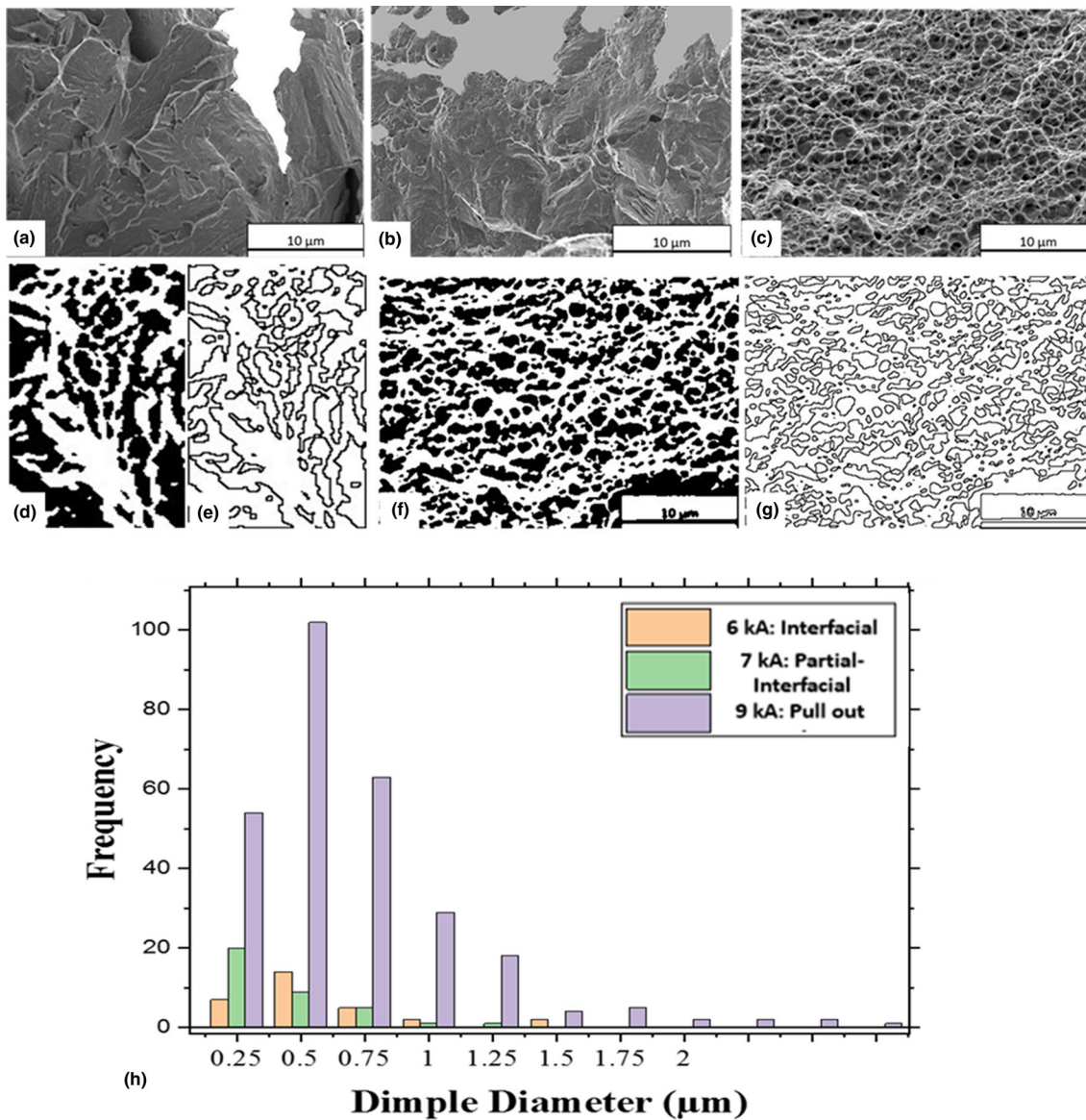


Fig. 11 Illustration of steps involved in quantitative fractography of tensile-shear tested specimens welded at different current: (a) fractography of 6 kA current sample with distinguished ductile and brittle zones, (b) fractography of 7 kA current sample with distinguished ductile and brittle zones, (c) fully ductile fracture in 9 kA current sample, (d) selected ductile zone in 6 kA specimen, (e) its image processing for quantification of dimple size distribution, (f, g) processed images of 9 kA current sample, (h) frequency distribution plot of dimple diameter for ductile zones of tensile-shear tested specimens corresponding to 6, 7 and 9 kA welding current

mode from interfacial to partial interfacial fracture. On increasing the welding current further to 9 kA, there was a 100% ductile fracture corresponding to pull-out failure as shown in Fig. 11(c).

In addition to the fraction of ductile fracture, the size distribution of dimples can have a significant impact on the work hardening capability and ductility of steel (Ref 47). Several works describe in detail the methodology for quantitative fractography deploying Image J software (Ref 47-49). In the present work, ductile zones of interfacial and partial interfacial fracture were separated and dimple size analysis was carried out as shown in Fig. 11(d-e). A similar exercise was carried out for pull-out fracture; however, it did not require any

separation of ductile fracture zone as there was no region of transgranular cleavage fracture. Figure 11(f-g) shows the processed fractography image of complete pull-out failure. A quantitative summary of the ductile fracture regions in case of interfacial, partial-interfacial, and pull-out failures in terms of the frequency distribution of dimple sizes is presented in Fig. 11(h). The total number of dimples is the highest in the case of pull-out fracture followed by partial-interfacial fracture and is the minimum in case of interfacial failure. This is consistent with the area fraction of ductile zone in these failure modes. Secondly, all the fractures showed a normal distribution skewed to the right. It is interesting to note that no dimple could grow larger than 1.5 μm in case of both interfacial and partial

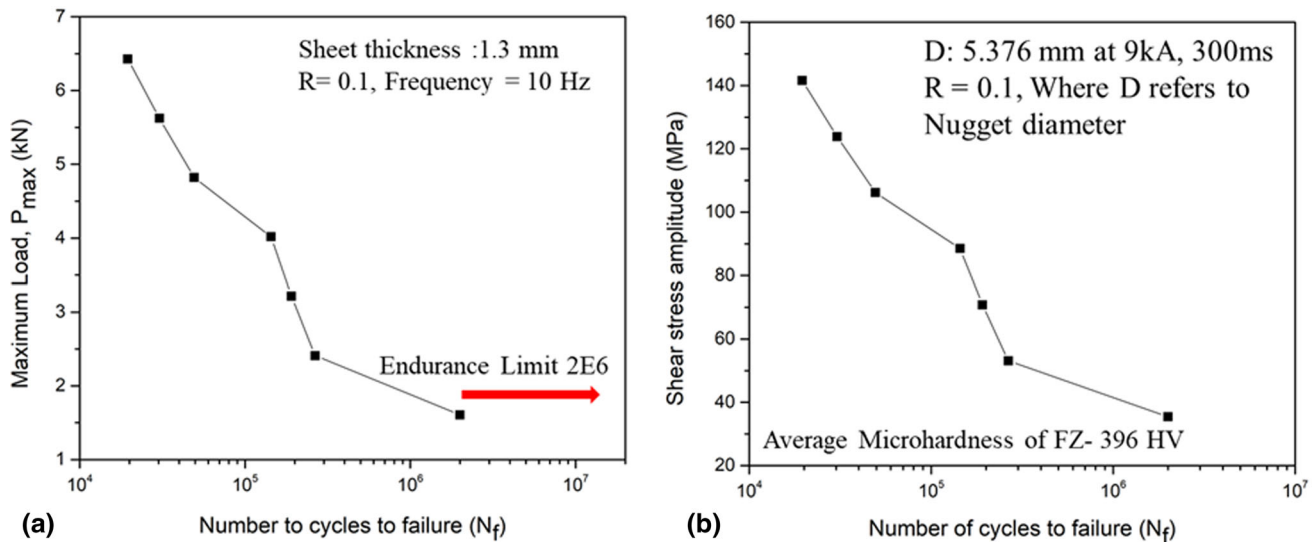


Fig. 12 (a) Fatigue plot (P-N) for spot-welded specimens, (b) variation of number of cycles to failure with shear stress amplitude

interfacial failures. In contrast, pull-out failure mode allowed the coalescence and growth of dimples to a diameter greater than $1.5 \mu\text{m}$ as well. Some of the dimples had $\sim 5 \mu\text{m}$ diameter. Such a difference in the upper limit of the dimple diameter in the case of interfacial and pull-out modes can be related to the speed of crack growth in these cases. Despite carrying out all the experiments at the same cross-head velocity, interfacial and partial interfacial fractures having ~ 93 and $\sim 83\%$ of the fracture surface having transgranular brittle fracture features and would have fractured much faster, as it is believed that cracks can propagate nearly at the speed of the sound in case of brittle fracture (Ref 50). This would have allowed much lesser time for dimples in the ductile region to coalesce and grow adequately. In contrast, pull-out failure having complete ductile fracture features and much lower velocity of crack propagation would have allowed much greater time for dimple coalescence and growth and therefore, it is reflected in the high size fraction of certain dimples in this case.

3.5 Fatigue Behavior of Spot-Welded Joints

Fatigue tests of spot-welded sample for optimum welding condition (welding current of 9 kA with a welding time of 300 ms) were carried out with R -ratio (P_{min}/P_{max}) of 0.1 and frequency of 5 Hz at different percentages (10, 15, 20, 25, 30, 35, and 40%) of maximum load (17.49 kN) obtained in tensile-shear tests. The samples were subjected to sinusoidal load waveform. The fatigue test results with different input parameters and a corresponding number of cycles to failure are provided in the Supplementary file (S_Table 1) and the fatigue tested samples are shown in S_Figure 1.

Unlike the S-N curve for stress-controlled fatigue of conventional samples, the P-N (maximum load – number of cycles to failure) curve is usually plotted for resistance spot welded samples. This is due to the difficulty associated with the

calculation of stress amplitude in lap configuration. However, shear stress can be calculated as follows (Ref 51):

$$\tau = \frac{4P_{max}}{\pi D^2}$$

Here τ refers to shear stress acting on the cross section of the joint (MPa), P_{max} refers to maximum load (N), and D refers to nugget diameter (mm).

Figure 12(a) represents fatigue life plot between maximum load with a number of cycles to failure at spot-welded joints fabricated at 9 kA welding current and 300 ms welding time. It was observed that the number of cycles to failure increases with a decrease in the maximum load. It is evident that for a small decrease in the maximum load, there is a large increase in the number of cycles to failure, elucidating the key role of the in-service maximum stress on the performance of the spot welded joints. An endurance was reached for the maximum load value of 1.74 kN, which is 10% of the peak load in the tensile-shear test. The work highlights that designing the weld only based on tensile-shear tests may be misleading as for the cyclic load as low as 15% of the tensile-shear load-bearing capacity can result in fatigue failure in less than 0.3 million cycles. Figure 12(b) shows that similar to the P-N plot, the dependence of the number of cycles to failure showed an increasing trend with a decrease in the magnitude of shear stress amplitude.

3.6 Fractography of Fatigue Tested Samples

Fractography of all the fatigue-tested specimens as shown in Fig. 13 revealed characteristic fatigue striations. Each striation spacing represents the distance moved by the crack in one cycle of loading and unloading (Ref 52, 53). Generally, at lower values of maximum load, the striation spacings are finer whereas, at higher loads, the width of striations is greater.

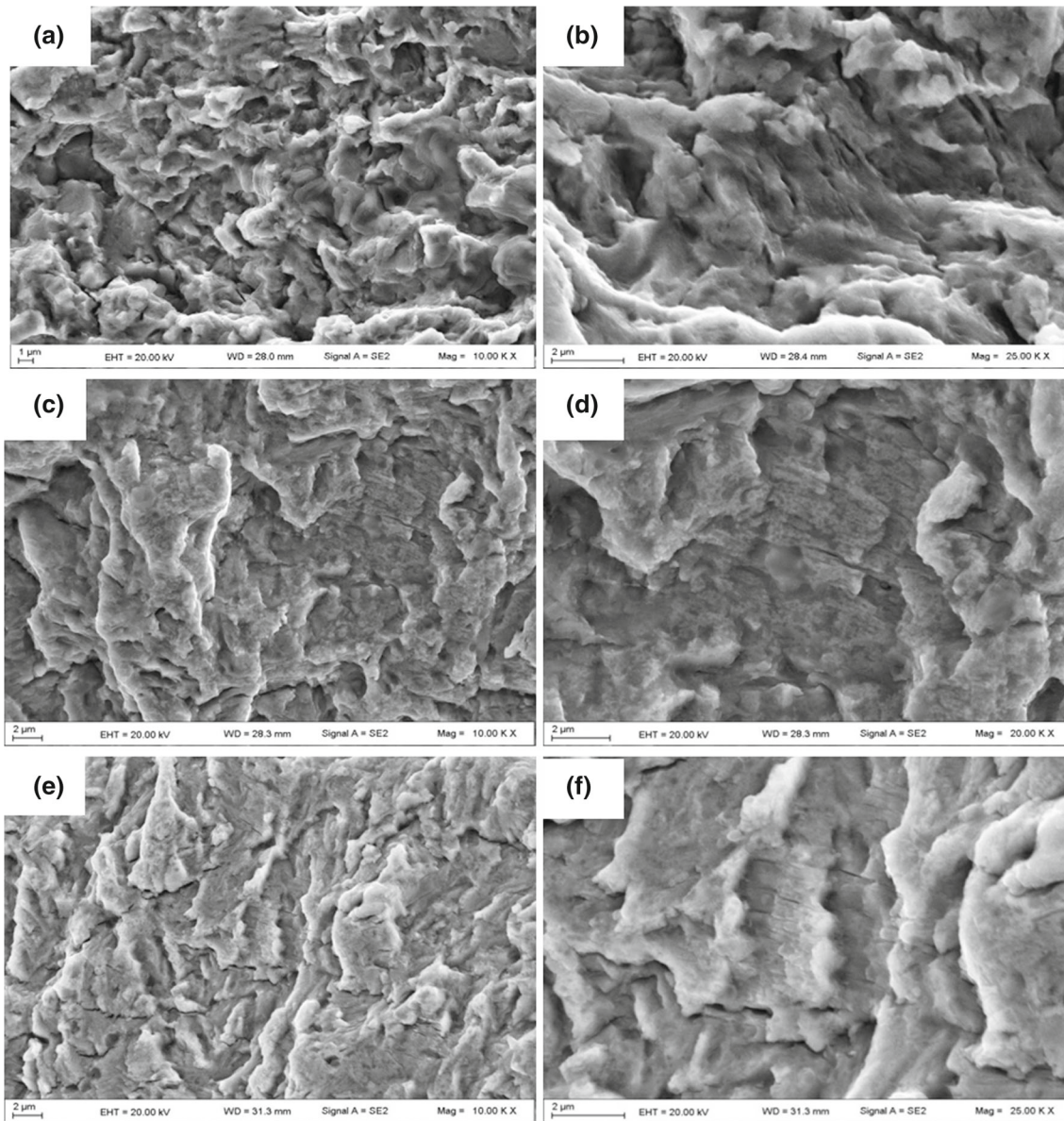


Fig. 13 SEM fractography of fatigue tested specimens at different fractions of maximum load in tensile-shear tests: (a, b) 15%, (c, d) 30%, (e, f) 40%

Furthermore, at higher loads, some secondary cracks were also observed.

3.7 Crack Initiation and Propagation under Tensile-Shear and Fatigue Tests

Microstructure-crack path interaction of spot-welded specimens at lower and higher welding currents in tensile-shear tests is presented in Fig. 14. At lower welding current (7 kA), crack initiated at the interface of the sheet metals and propagated toward the nugget into the heat-affected zone as shown in Fig. 14(a). Subsequently, crack propagated in the thickness direction in the coarse-grained heat affected zone which consisted of martensitic microstructure as depicted in

Fig. 14(b). A higher strain localization may have assisted in easier crack propagation in CGHAZ. Figure 14(c) shows that at a higher welding current (9 kA), crack initiated near the tongue of the sheet metal interface and then did not propagate much inside the heat-affected zone. Instead, it propagated in the thickness direction around the base metal/heat-affected zone interface. Such a difference in the crack path on changing the welding current may explain the signatory fractographic features in the two cases. A predominantly brittle cleavage fracture was observed at a lower current (7 kA) owing to the crack propagation through coarse-grained heat affected zone having relatively brittle martensite. In contrast, crack propagation through tough ferrite-martensite microstructure can explain the occurrence of ductile dimples in the tensile-shear tested

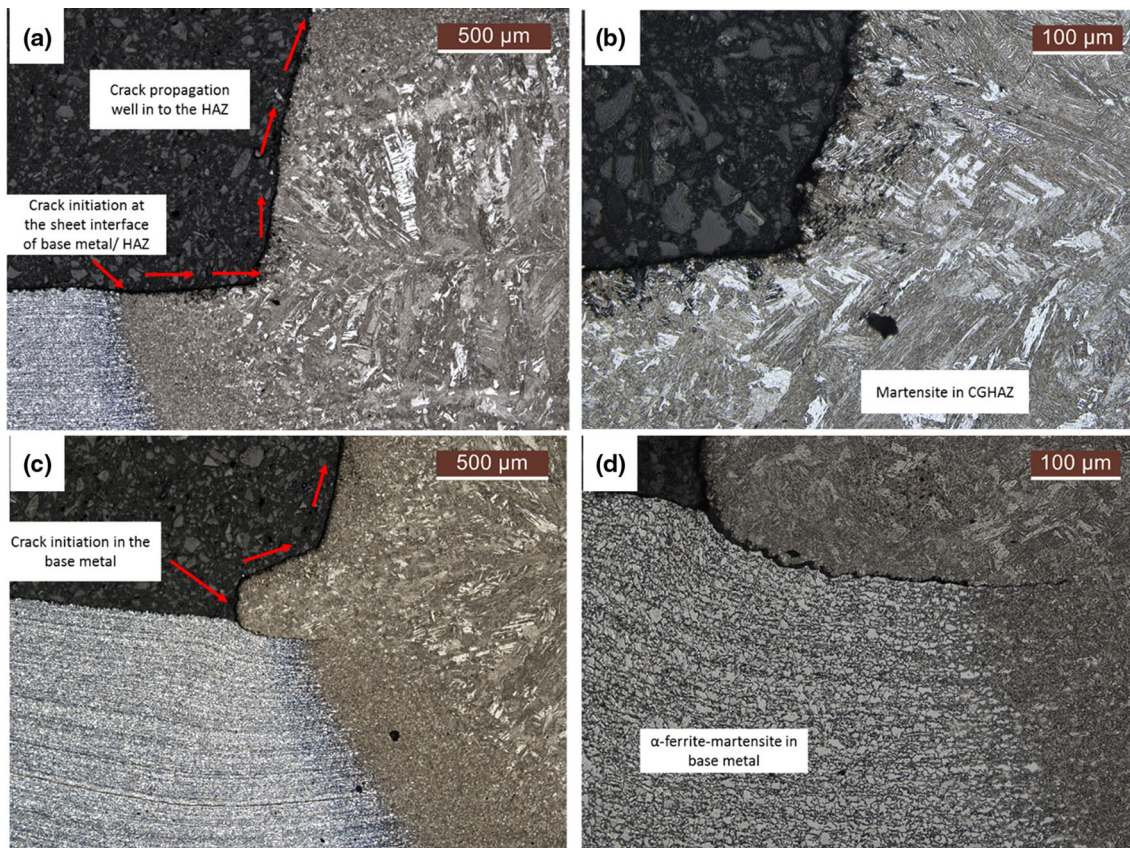


Fig. 14 Optical micrograph showing crack path in tensile-shear tests for (a, b) low welding current (7 kA), (c, d) high welding current (9kA)

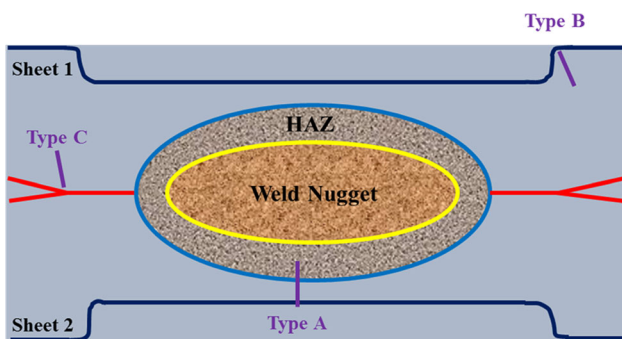


Fig. 15 Schematic representation of different categorizations of liquid metal embrittlement (LME) cracks

specimens at higher current (9 kA). This microstructural aspect plays a synergistic role in the factor that at higher welding current there is greater nugget diameter, which reduces the shear stress and directs the crack to propagate around the nugget rather than through it.

Liquid metal embrittlement (LME) has been reported to be a prominent problem during the resistance spot welding of zinc-coated high strength steels (Ref 54-57). It has been shown that the susceptibility to LME increases with an increase in the strength of the steel. During RSW of zinc-coated steel, liquid zinc can segregate around grain boundaries and cause embrittlement (Ref 58). Alternatively, stress-induced diffusion of zinc

due to electrode force and heat input from welding is also proposed as a mechanism for LME in RSW (Ref 59). In the case of RSW, LME cracks are classified into three categories, namely Type A, Type B, and Type C as shown in Fig. 15 (Ref 54). Type A crack which occurs around the weld zone, usually above the nugget or indent was not observed in the present case. Furthermore, no crack around the shoulder of the electrode indentation area was observed to suggest the occurrence of type B LME, which is the most commonly reported in RSW processes (Ref 60-62). Detailed optical metallography around the shoulder region of the electrode indentation is presented in Fig. 16(a) and (b) to show an absence of LME cracks. Magnified SEM image around the ICHAZ, where the temperature range is such that it is most vulnerable to LME is shown in Fig. 16(c). Cross section EDS line analysis is shown in Fig. 16(d) revealed that the zinc coating was intact.

Figure 17(a) and (b) shows the crack path in fatigue-tested specimens at lower (1.18 kN) and higher (3.14 kN) values of load amplitudes, respectively. As discussed earlier, these tests were conducted at welding parameters that yielded the maximum tensile-shear load-bearing capacity and failed in favorable pull-out failure mode during the tensile-shear tests. As evidenced from Fig. 17(a) and (b), fatigue cracks have initiated at the sheet metal interface in the heat-affected zone and propagated in the thickness direction. This is contrary to the tensile-shear test of the specimen welded at a similar parameter, where the crack had initiated in the base metal. Similar observations on the difference in failure mechanisms

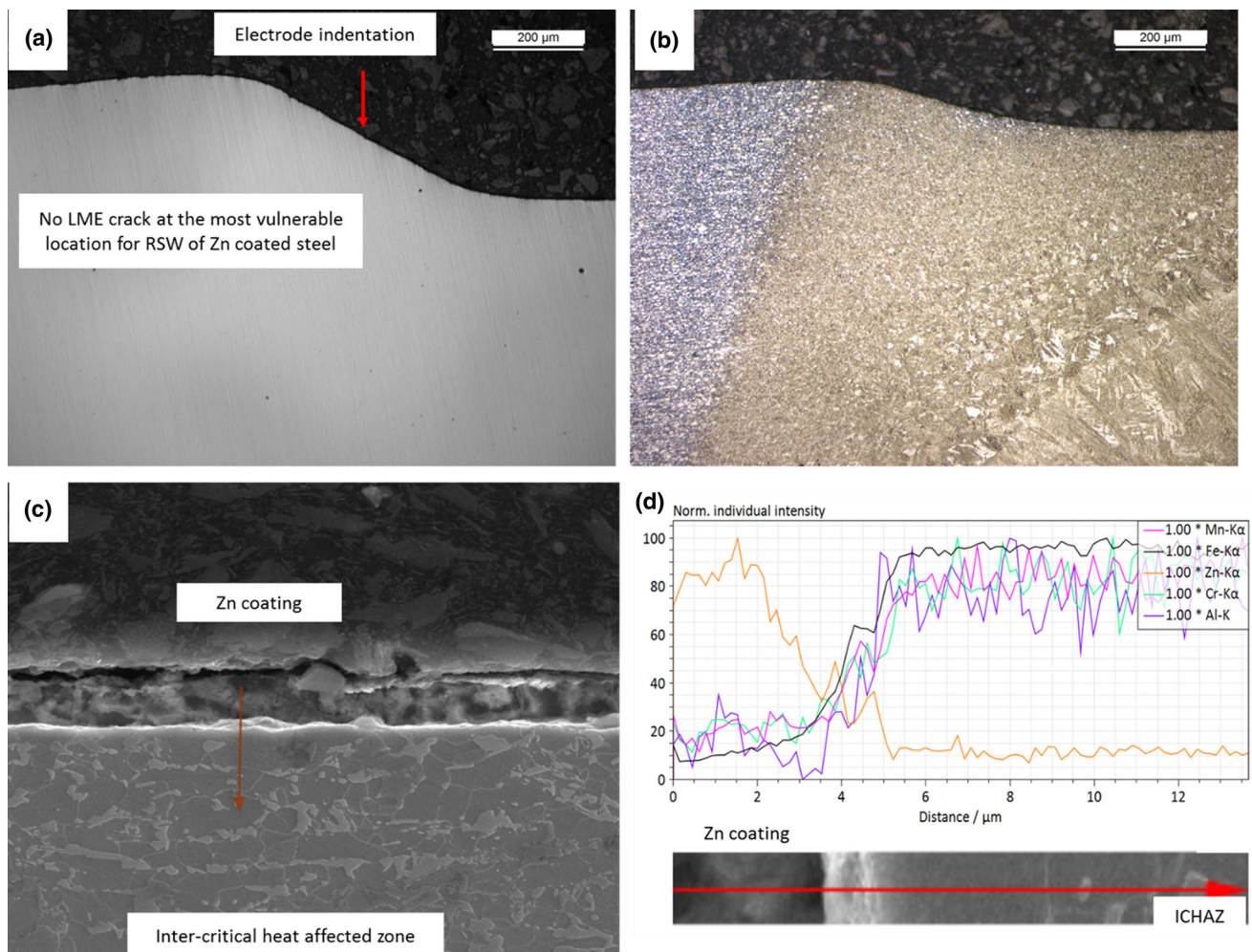


Fig. 16 Micrographs investigating the possibility of Type B LME crack in the spot-welded sheet: (a) un-etched micrograph near the electrode indentation shoulder, (b) etched micrograph, (c) magnified SEM image showing coating free of any LME crack, (d) EDS compositional analysis across the coating thickness in the ICHAZ.

during tensile-shear and fatigue tests at optimum welding parameter have been reported for high strength low alloy and dual phase-interstitial free steel spot welds (Ref 38, 63). However, it is worth noting that the fatigue specimen that was tested at higher load amplitude showed multiple fatigue cracks initiation around the sheet metal interface which was not observed in the low amplitude tested specimen. As shown in Fig. 17(c), (d), the length of these cracks varied between 5 and 20 μm . Elemental mapping of these cracks presented in Fig. 18 showed presence of zinc within them.

4. Conclusions

The effect of welding current on load-bearing capacity, the mode, and the mechanism of failure under tensile-shear loading conditions for zinc-coated DP 600 steel has been established in

this study. Subsequently, fatigue tests at the optimum welding current have been carried out to understand the differences in the crack initiation and propagation path under quasi-static and cyclic loading conditions, which are both experienced by spot-welded joints in the actual service conditions. Following are the major conclusions from this study:

1. An increase in welding current has a profound impact on the tensile-shear load-bearing ability as suggested by a greater than three-fold increase in the load-bearing capacity for specimen welded at 9 kA current compared to that welded at 6 kA current.
2. Welding current influences both macroscopic and microscopic mechanisms of failure. With an increase in welding current, a transition in failure mode from interfacial, to partial-interfacial and eventually pull-out mode was observed. These macroscopic transitions corroborated with transitions in micro-mechanism of fracture with pre-

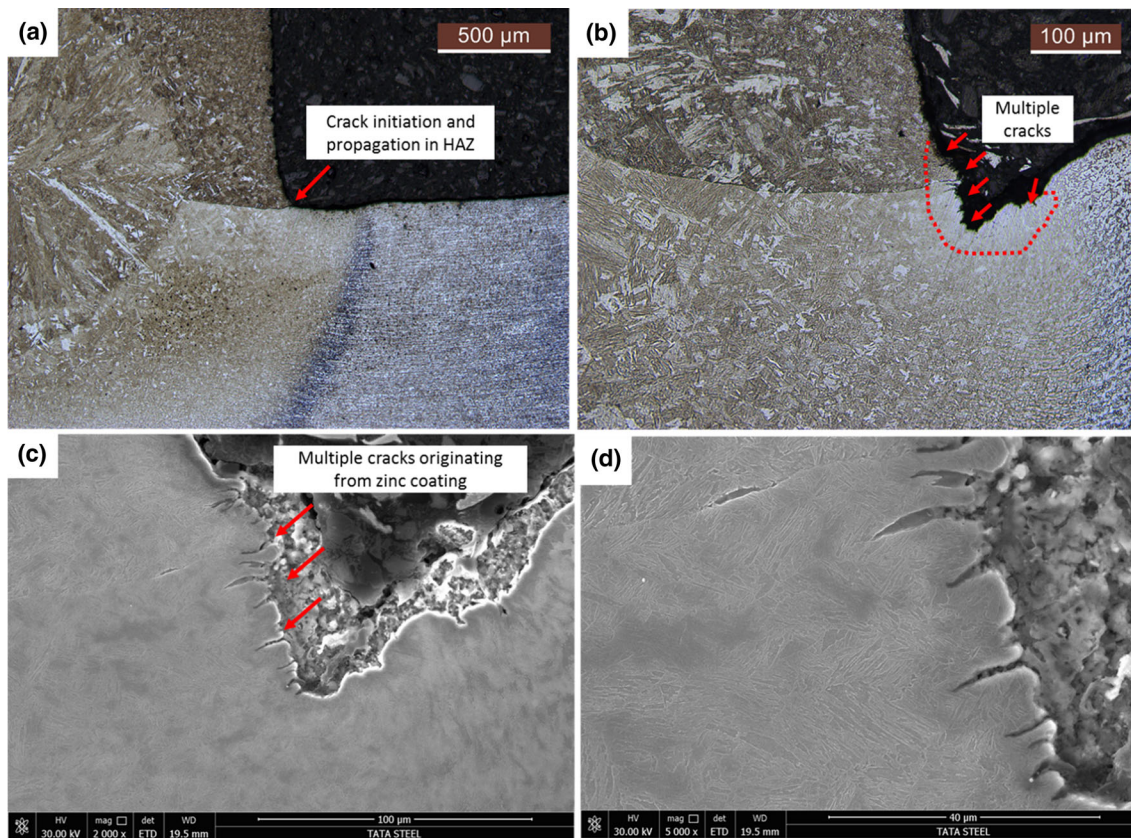


Fig. 17 (a, b) Optical micrographs showing the crack path in fatigue tests, (c) Sheet metal interface showing multiple cracks, (d) magnified view of the cracks in the fatigue tested specimen

- dominantly cleavage fracture for interfacial failure to fully ductile fracture corresponding to pull-out failure.
3. Quantitative fractography revealed that there was an increase in the fraction of ductile fracture from 7.6 to 17.1% on the transition from interfacial to partial-interfacial failure. Eventually, for complete pull-out failure, 100% ductile dimples were observed. Interestingly, the fraction of coarser dimples increased with an increase in welding current due to greater available time for their coalescence and growth.
 4. Fatigue tests at optimum welding current revealed an increase in a number of cycles to failure with decreasing load amplitude.
 5. At the optimum welding parameter, a difference in crack initiation and propagation mechanisms was observed for tensile-shear and fatigue tests. Whereas the crack initiated at the base metal and propagated around the nugget in the optimum parameter in quasi-static tests, fatigue crack(s) initiated at or around the sheet metal interface having high-stress concentration and propagated inside the heat-affected zone. Further, compared to single crack initiation and propagation under tensile-shear tests, multiple microscopic cracks associated with zinc were observed for fatigue-tested specimens, especially at higher load amplitude. In general, RSW galvanized DP600 steel sheets did not show a prominent tendency for liquid metal embrittlement (LME).

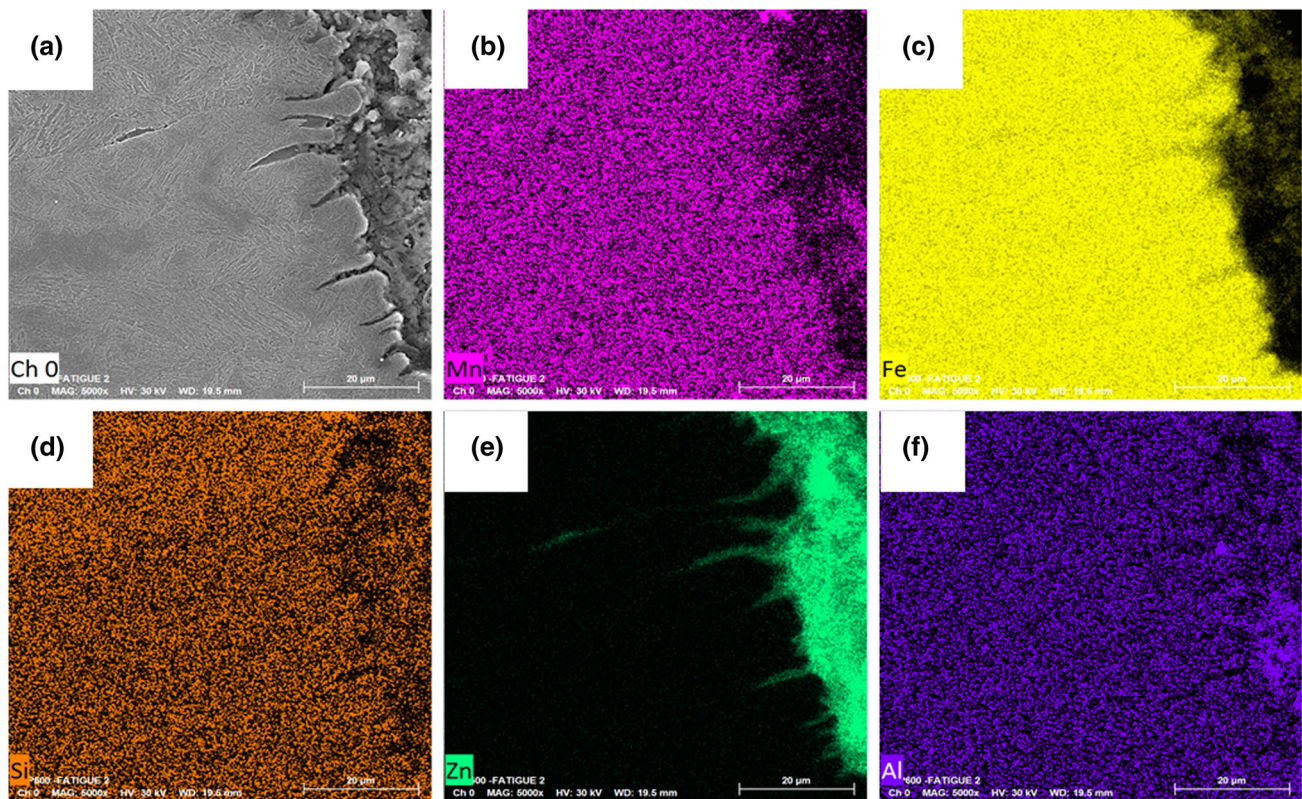


Fig. 18 (a) SEM image showing multiple fatigue cracks, elemental mapping showing the variation of different elements: (b) Mn, (c) Fe, (d) Si, (e) Zn, (f) Al

References

1. D.K. Matlock, J.G. Speer, E. De Moor and P.J. Gibbs, Recent Developments in Advanced High Strength Sheet Steels for Automotive Applications: An Overview, *Jestech*, 2012, **15**, p 1–12.
2. R. Rana, S.B. Singh, *Automotive Steels: Design, Metallurgy, Processing and Applications*, first ed. 2016
3. J.H. Schmitt and T. Lung, New Developments of Advanced High-Strength Steels for Automotive Applications, *C R Phys.*, 2018, **19**(8), p 641–656.
4. A. Kalhor, M. Soleimani, H. Mirzadeh and V. Uthaisangskul A review of recent progress in mechanical and corrosion properties of dual phase steels, *Arch. Civ. Mech. Eng.*, 2020, **85**
5. N. Fonstein, *Dual-phase Steels (in Automotive Steels: Design, Metallurgy, Processing and Applications)*, first ed., 2016, pp 169–216
6. A. Chakraborty, M. Adhikary, T. Venugopalan, V. Singh, T. Nanda and B.R. Kumar, Effect of Ferrite-Martensite Interface Morphology on Bake Hardening Response of DP590 Steel, *Mater. Sci. Eng., A*, 2016, **676**, p 463–473.
7. H. Seydrezain, A.K. Pilkey and J.D. Boyd, Effect of Pre-IC Annealing Treatments on the Final Microstructure and Work Hardening Behavior of a Dual-Phase Steel, *Mater. Sci. Eng., A*, 2014, **594**, p 178–188.
8. Y. Cao, J. Ahlström and B. Karlsson, The Influence of Temperatures and Strain Rates on the Mechanical Behavior of Dual Phase Steel in Different Conditions, *J. Mater. Technol.*, 2015, **4**, p 68–74.
9. A. Chakraborty, M. Dutta, R. Pais and R.K. Ray, Analysis of an Uncommon Coating Defect on Industrial Galvannealed High Strength Interstitial Free Steel, *Surf. Coat. Technol.*, 2010, **204**, p 3481–3489. <https://doi.org/10.1016/j.surfcoat.2010.04.020>
10. M.S. Khan, S.D. Bhole, D.L. Chen, E. Biro, G. Boudreau and J. van Deventer, Welding Behaviour, Microstructure and Mechanical Properties of Dissimilar Resistance Spot Welds Between Galvannealed HSLA350 and DP600 Steels, *Sci. Technol. Weld. Join.*, 2009, **14**(7), p 616–625. <https://doi.org/10.1179/136217109X12464549883295>
11. M. Pouranvari and S.P.H. Marashi, Critical Review of Automotive Steels Spot Welding: Process, Structure and Properties, *Sci. Technol. Weld. Joining*, 2013, **18**(5), p 361–403. <https://doi.org/10.1179/1362171813Y.0000000120>
12. A. De, Spot Welding, *Sci. Technol. Weld. Joining*, 2008, **13**, p 213–214.
13. N.T. Williams and J.D. Parker, Review of Resistance Spot Welding of Steel Sheets: Part 1 – Modelling and Control of Weld Nugget Formation, *Int. Mater. Rev.*, 2004, **49**, p 45–75.
14. G. Janardhan, K. Kishore, K. Dutta and G. Mukhopadhyay, Tensile and Fatigue Behavior of Resistance Spot Welded HSLA Steel Sheet: Effect of Pre-strain in Association with Dislocation Density, *Mater. Sci. Eng., A*, 2020, **793**, 139796. <https://doi.org/10.1016/j.msea.2020.139796>
15. I. Hajiannia, M. Shamanian, M. Atapour and R. Ashiri, Evaluation of Weldability and Mechanical Properties in Resistance Spot Welding of Ultrahigh-Strength TRIP1100 Steel, *SAE Int. J. Mater. Manuf.*, 2018, **12**(1), p 5–18. <https://doi.org/10.4271/05-12-01-0001>
16. W. Xu, D. Chen, L. Liu, H. Mori and Y. Zhou, Microstructure and Mechanical Properties of Weld-Bonded and Resistance Spot Welded Magnesium-to-Steel Dissimilar Joints, *Mater. Sci. Eng., A*, 2012, **537**, p 11–24. <https://doi.org/10.1016/j.msea.2011.12.096>
17. Z. Ling, T. Chen, L. Kong, M. Wang and H. Pan, Liquid Metal Embrittlement Cracking During Resistance Spot Welding of Galvanized Q&P980 Steel, *Mater. Sci. Eng., A*, 2019, **50**(11), p 1–15. <https://doi.org/10.1007/s11661-019-05388-6>
18. D. Bhattacharya, Liquid Metal Embrittlement during Resistant Spot Welding of Zn-Coated High-Strength Steels, *Mater. Sci. Technol.*, 2018, **34**(1), p 1–21. <https://doi.org/10.1080/02670836.2018.1461595>
19. Z. Ling, M. Wang, L. Kong and K. Chen, Towards an Explanation of Liquid Metal Embrittlement Cracking in Resistance Spot Welding of Dissimilar Steels, *Mater. Des.*, 2020, **195**, p 1–14. <https://doi.org/10.1016/j.matdes.2020.109055>
20. R. Chen, C. Zhang, M. Lou, Y. Li and B.E. Carlson, Effect of Al-Si Coating on Weldability of Press-Hardened Steels, *J. Mater. Eng. Perform.*, 2020, **29**(1), p 626–636. <https://doi.org/10.1007/s11665-020-04555-w>
21. R. Ashiri, M.A. Haque, C.W. Ji, M. Shamanian, H.R. Salimijazi and Y.D. Park, Supercritical Area and Critical Nugget Diameter for Liquid Metal Embrittlement of Zn-Coated Twinning Induced Plasticity Steel,

- Scr. Mater.*, 2015, **109**, p 6–10. <https://doi.org/10.1016/j.scrptamat.2015.07.006>
22. R. Ashiri, M. Shamanian, H.R. Salimijazi, M.A. Haque, J.H. Bae, C.W. Ji, K.J. Chin and Y.D. Park, Liquid Metal Embrittlement-Free Welds of Zn-Coated Twinning Induced Plasticity Steels, *Scr. Mater.*, 2016, **114**, p 41–47. <https://doi.org/10.1016/j.scrptamat.2015.11.027>
 23. R. Ashiri, H. Mostaan and Y.D. Park, A Phenomenological Study of Weld Discontinuities and Defects in Resistance Spot Welding of Advanced High Strength TRIP Steel, *Metall. Mater. Trans. A.*, 2018, **49**, p 6161–6172. <https://doi.org/10.1007/s11661-018-4900-0>
 24. M. Milititsky, E. Pakalnins, C. Jiang and A.K. Thompson, On Characteristics of DP600 Spot Welding, SAE Transactions, *J. Mater. Manuf.*, 2003, **112**(5), p 244–251.
 25. M. Pouranvari, Effect of Welding Parameters on the Peak Load and Energy Absorption of Low-Carbon Steel Resistance Spot Welds, *Int. Sch. Res. Notices.*, 2011, **2011**, p 1–7. <https://doi.org/10.5402/2011/824149>
 26. M. Pouranvari and S.P.H. Marashi, Key Factors Influencing Mechanical Performance of Dual Phase Steel Resistance Spot Welds, *Sci. Technol. Weld. Join.*, 2010, **15**(2), p 149–155. <https://doi.org/10.1179/136217109X12590746472535>
 27. K. Kishore, P. Kumar and G. Mukhopadhyay, Resistance Spot Weldability of Galvannealed and Bare DP600 Steel, *J. Mater. Process. Technol.*, 2019, **271**, p 237–248. <https://doi.org/10.1016/j.jmatprotec.2019.04.005>
 28. C. Ma, D.L. Chen, S.D. Bhole, G. Boudreau, A. Lee and E. Biro, Microstructure and Fracture Characteristics of Spot-Welded DP600 Steel, *Mater. Sci. Eng., A*, 2008, **485**, p 334–346. <https://doi.org/10.1016/j.msea.2007.08.010>
 29. C.A.N. Lanzillotto and F.B. Pickering, Structure Property Relationships in Dual-Phase Steels, *Met. Sci.*, 1982, **16**, p 371–382.
 30. J.C. Bittence, Dual-Phase Steels Promise Higher Strength Plus Formability, *Mater. Eng.*, 1978, **87**, p 39–42.
 31. M. Balbi, I. Alvarez-Armas and A. Armas, Effect of Holding Time at an Inter-critical Temperature on the Microstructure and Tensile Properties of a Ferrite–Martensite Dual Phase Steel, *Mater Sci Eng A.*, 2018, **733**, p 1–8.
 32. D. Das and P.P. Chattopadhyay, Influence of Martensite Morphology on the Work-Hardening Behavior of High Strength Ferrite–Martensite Dual-Phase Steel, *J Mater Sci.*, 2009, **44**, p 2957–2965.
 33. L.E. Svensson and J.K. Larsson, Welding and Joining of High Performance Car Bodies, *Steel World (UK)*, 2002, **7**(7), p 21–32.
 34. G. Janardhan, G. Mukhopadhyay, K. Kishore and K. Dutta, Resistance Spot Welding of Dissimilar Interstitial-Free and High-Strength Low-Alloy Steels, *J. Mater. Eng. Perform.*, 2020, **29**, p 3383–3394. <https://doi.org/10.1007/s11665-020-04857-z>
 35. M.D. Tumuluru, Resistance Spot Welding of Coated High Strength Dual-Phase Steels, *Weld. J.*, 2006, **85**, p 31–37.
 36. X. Sun, E.V. Stephens and M.A. Khaleel, Effects of Fusion Zone Size and Failure Mode on Peak Load and Energy Absorption of Advanced High Strength Steel Spot Welds under Lap Shear Loading Conditions, *Eng. Fail. Anal.*, 2008, **15**(4), p 356–367. <https://doi.org/10.1016/j.engfailanal.2007.01.018>
 37. BS 1140:1993, Specification for resistance spot welding of uncoated and coated low carbon steel. British standard. 1993, ISBN: 0-580-21944-5
 38. K. Kishore, P. Kumar and G. Mukhopadhyay, Microstructure, Tensile and Fatigue Behaviour of Resistance Spot Welded Zinc Coated Dual Phase and Interstitial Free Steel, *Met. Mater. Int.*, 2021 <https://doi.org/10.1007/s12540-020-00939-8>
 39. P. Zhang, J. Xie, Y.X. Wang and J.Q. Chen, Effect of Welding Parameters on Mechanical Properties and Microstructure of Resistance Spot Welded DP600 Joints, *Sci. Technol. Weld. Join.*, 2011, **16**(7), p 567–574. <https://doi.org/10.1179/136217110X12813393169732>
 40. M. Pouranvari, Susceptibility to Interfacial Failure Mode in Similar and Dissimilar Resistance Spot Welds of DP600 Dual Phase Steel and Low Carbon Steel during Cross Tension and Tensile-Shear Loading Conditions, *Mater. Sci. Eng., A*, 2012, **546**, p 129–138. <https://doi.org/10.1016/j.msea.2012.03.040>
 41. M. Tamizi, M. Pouranvari and M. Movahedi, The Role of HAZ Softening on Cross-Tension Mechanical Performance of Martensitic Advanced High Strength Steel Resistance Spot Welds, *Metall. Mater. Trans. A.*, 2021, **52**(2), p 655–667. <https://doi.org/10.1007/s11661-020-06104-5>
 42. I. Hajiannia, M. Shamanian, M. Atapour, E. Ghassemali and R. Ashiri, A Microstructure Evaluation of Different Areas of the Resistance Spot Welding on New Advanced Ultra-High Strength TRIP1100 Steel, *Cogent Eng.*, 2018, **5**(1), p 1–13. <https://doi.org/10.1080/23311916.2018.1512939>
 43. M. Pouranvari, S. Sobhani and F. Goodarzi, Resistance Spot Welding of MS1200 Martensitic Advanced High Strength Steel: Microstructure-Properties Relationship, *J. Manuf. Process.*, 2018, **31**, p 867–874. <https://doi.org/10.1016/j.jmapro.2018.01.009>
 44. S. Vignier, E. Biro and M. Herve, Predicting the Hardness Profile Across Resistance Spot Welds in Martensitic Steels, *Weld World*, 2014 <https://doi.org/10.1007/s40194-014-0116-0>
 45. M.I. Khan, M.L. Kuntz, E. Biro and Y. Zhou, Microstructure, and Mechanical Properties of Resistance Spot Welded Advanced High Strength Steels, *Mater. Trans.*, 2008, **49**(7), p 1629–1637. <https://doi.org/10.2320/matertrans.MRA2008031>
 46. R. Blondeau, Mathematical Model for the Calculation of Mechanical Properties of Low-Alloy Steel Metallurgical Products, *Heat Treat.*, 1976, **76**, p 189–200.
 47. K. Kishore, R.G. Kumar and A.K. Chandan, Critical Assessment of the Strain-Rate Dependent Work Hardening Behaviour of AISI 304 Stainless Steel, *Mater. Sci. Eng. A*, 2021 <https://doi.org/10.1016/j.msea.2020.140675>
 48. A. Das and S. Tarafder, Experimental Investigation on Martensitic Transformation and Fracture Morphologies of Austenitic Stainless Steel, *Int. J. Plast.*, 2009, **25**, p 2222–2247. <https://doi.org/10.1016/j.ijplas.2009.03.003>
 49. A. Das and S. Tarafder, Geometries of Dimples and Its Correlation with Mechanical Properties in Austenitic Stainless Steel, *Scr. Mater.*, 2008, **59**(9), p 1014–1017. <https://doi.org/10.1016/j.scrptamat.2008.07.012>
 50. B.A. Miller, Overload Failures, *Failure Analysis and Prevention*. W.T. Becker, R.J. Shipley Ed., ASM International, 2002, p 671–699. <https://doi.org/10.31399/asm.hb.v11.a0003543>
 51. D. Zhao, Y. Wang, D. Liang and P. Zhang, Modelling and Process Analysis of Resistance Spot Welded DP600 Joint Based on Regression Analysis, *Mater. Des.*, 2016, **110**, p 676–684. <https://doi.org/10.1016/j.matdes.2016.08.038>
 52. G.E. Dieter, *Mechanical Metallurgy*, 3rd ed. McGraw-hill, New York, 1986
 53. K. Kishore and M. Adhikary, Metallurgical Investigation and Life Cycle Assessment of a Piston Rod of Thin Slab Caster, *J. Fail. Anal. Prev.*, 2019, **19**, p 1407–1419. <https://doi.org/10.1007/s11668-019-00738-3>
 54. M.H. Razmpoosh, C. DiGiovanni, Y.N. Zhou and E. Biro, Pathway to Understand Liquid Metal Embrittlement (LME) in Fe-Zn Couple: From Fundamentals Toward Application, *Prog. Mater. Sci.*, 2021, **121**, p 100798. <https://doi.org/10.1016/j.pmatsci.2021.100798>
 55. J. Frei, M. Biegler, M. Rethmeier, C. Böhne and G. Meschut, Investigation of Liquid Metal Embrittlement of Dual Phase Steel Joints by Electro-Thermomechanical Spot-Welding Simulation, *Sci. Technol. Weld. Join.*, 2019, **24**(7), p 1–10. <https://doi.org/10.1080/13621718.2019.1582203>
 56. M.H. Razmpoosh, A. Macwan, F. Goodwin, E. Biro and Y. Zhou, Crystallographic Study of Liquid-Metal-Embrittlement Crack Path, *Mater. Lett.*, 2020, **267**, p 127511.
 57. H. Lee, M.C. Jo, S.S. Sohn, S.H. Kim, T. Song, S.K. Kim, H.S. Kim, N.J. Kim and S. Lee, Microstructural Evolution of Liquid Metal Embrittlement in Resistance-Spot-Welded Galvanized Twinning-Induced Plasticity (TWIP) Steel Sheets, *Mater. Charact.*, 2019, **147**, p 233–241. <https://doi.org/10.1016/j.matchar.2018.11.008>
 58. S.P. Murugan, V. Vijayan, C. Ji and Y. Park, Four Types of LME Cracks in RSW of Zn-Coated AHSS, *Weld. J.*, 2020, **99**(3), p 75–92.
 59. K. Kwon, G. Jang, W. Kim, S. Uhm, T. Lee and C. Lee, Effect of Type-C Liquid Metal Embrittlement on Mechanical Properties of Spot-Welded TRIP Steel, *J. Market. Res.*, 2021, **13**, p 2482–2490. <https://doi.org/10.1016/j.jmrt.2021.06.041>
 60. K. Mahmud, S.P. Murugan, Y. Cho, C. Ji, D. Nam and Y. Park, Geometrical Degradation of Electrode and Liquid Metal Embrittlement Cracking in Resistance Spot Welding, *J. Manuf. Process.*, 2021, **61**, p 334–348. <https://doi.org/10.1016/j.jmapro.2020.11.025>
 61. O. Siar, Y. Benlatreche, T. Dupuy, S. Dancette and D. Fabrègue, Effect of Severe Welding Conditions on Liquid Metal Embrittlement of a 3rd-Generation Advanced High-Strength Steel, *Metals*, 2020, **10**(9), p 1166–1176. <https://doi.org/10.3390/met10091166>

62. D. Choi, A. Sharma, S. Uhm and J.P. Jung, Liquid Metal Embrittlement of Resistance Spot Welded 1180 TRIP Steel: Effect of Electrode Force on Cracking Behavior, *Met. Mater. Int.*, 2019, **25**, p 219–228. <https://doi.org/10.1007/s12540-018-0180-x>
63. G. Janardhan, K. Kishore, G. Mukhopadhyay and K. Dutta, Fatigue Properties of Resistance Spot Welded Dissimilar Interstitial-Free and

High Strength Micro-Alloyed Steel Sheets, *Met. Mater. Int.*, 2020 [h
https://doi.org/10.1007/s12540-020-00678-w](https://doi.org/10.1007/s12540-020-00678-w)

Publisher's Note Springer Nature remains neutral with regard to jurisdictional claims in published maps and institutional affiliations.